Synthesis, characterization, and biological activity of a fresh class of sonochemically synthesized Cu2+ complexes

scientific reports

Check for updates

OPEN

Synthesis, characterization, and biological activity of a fresh class of sonochemically synthesized Cu^{2+} complexes

Hamed Ghanbari[1], Hossein Derakhshankhah[2]✉, Kiumars Bahrami[1,3]✉, Saeide Keshavarzi[4], Khosro Mohammadi[4]✉, Payam Hayati[4,5]✉, Roberto Centore[6] & Emmanuele Parisi[6]

The synthesis and characterization of metal complexes have garnered significant attention due to their versatile applications in scientific and biomedical fields. In this research, two novel copper (Cu) complexes, $[Cu(L)(L')(H_2O)_2]$ (1) and $[Cu(L)(Im)H_2O]$ (2), where L = pyridine-2,6-dicarboxylic acid, L′ = 2,4-diamino-6-hydroxypyrimidine, and Im = imidazole, were investigated concerning their sonochemical synthesis, spectroscopic analysis, and biological activity. The complexes' structural characterization was achieved using analytical techniques, including single-crystal X-ray structure determination, FTIR, PXRD, TGA and DTA, SEM, TEM, and EDS. Complex (1) displayed a six-coordinated Cu^{2+} ion, while complex (2) exhibited a five-coordinated Cu^{2+} ion. The crystal structures revealed monoclinic (*C2/c*) and triclinic (*P*-1) space groups, respectively. Both complexes showcased zero-dimensional (0D) supramolecular networks, primarily driven by hydrogen bonding and π–π stacking interactions, which played pivotal roles in stabilizing the structures and shaping the unique supramolecular architecture. Both complexes demonstrated significant antioxidant activity, suggesting their capability to neutralize free radicals and mitigate oxidative stress-related diseases. Hemolysis percentages were less than 2%, per the ASTM F756-00 standard, indicating non-hemolytic behavior. Low cytotoxicity was observed against fibroblast and MCF-7 cell lines. They do not exhibit antibacterial activity against *Escherichia coli* and *Staphylococcus aureus*. These findings suggest that the synthesized Cu^{2+}—complexes hold considerable promise for applications in drug delivery and cancer treatment. This research contributes to the advancement of supramolecular chemistry and the development of multifunctional materials for diverse scientific and medical applications.

Keywords Supramolecular coordination complexes, Copper, Hemolysis, Antioxidant, Antibacterial, Cytotoxicity

Supramolecular chemistry, a field of study that investigates non-covalent molecular complexation, has rapidly gained attention in the scientific community, due to its potential for novel solutions to long-standing issues in various fields including biology, physics, engineering, and pharmacy[1]. This field encompasses the study of various types of intermolecular non-covalent bond formation in designed molecular systems, including dynamic covalent chemistry[2–4]. The term "supramolecular chemistry" was first coined in the 1970s by Jean-Marie Lehn[5], while the study of non-covalent molecular complexation was already under investigation within the scope of other scientific fields such as enzymology, organic chemistry, and inorganic chemistry[6–8]. Supramolecular chemistry offers an exciting opportunity for the development of new technologies and commercial products[4,9], and as such, has recently become an area of interest for the industry. The potential for supramolecular complexes to exhibit

[1]Department of Organic Chemistry, Faculty of Chemistry, Razi University, Kermanshah 67144-14971, Iran. [2]Pharmaceutical Sciences Research Center, Health Institute, Kermanshah University of Medical Sciences, Kermanshah, Iran. [3]Nanoscience and Nanotechnology Research Center (NNRC), Razi University, Kermanshah 67144-14971, Iran. [4]Department of Chemistry, Faculty of Sciences and Nano and Biotechnology, Persian Gulf University, Bushehr 75169, Iran. [5]Organic and Nano Group, Department of Chemistry, Iran University of Science and Technology, Tehran 16846-13114, Iran. [6]Department of Chemical Sciences, University of Naples Federico II, Via Cintia, 80126 Naples, Italy. ✉email: derakhshankhah.hossein@gmail.com; k.bahrami@razi.ac.ir; khmohammadi@pgu.ac.ir; payamhayati@yahoo.com

host–guest properties makes them attractive for a wide range of applications in catalysis[10], fluorescent probe design[11], and the development of novel theranostics and therapeutics[12]. Within the supramolecular coordination complexes (SCCs) family, 2D metallacycles and 3D cagelike structures, also defined as metallacages, are of particular interest due to their geometry, which generally allows an internal cavity to encapsulate guest molecules. The combination of covalent[13] and non-covalent[14] interactions allows precise control over the formation and properties of these compounds, enabling the design of functional materials with tailored properties, including van der Waals forces, hydrophobic effects, ion–dipole interactions, π–π stacking of aromatic rings, dipole–dipole interactions, tight packing in solids, ion–ion interactions, hydrogen bonding, chalcogen bonding, cation–π interactions, and anion–π interactions. The combination of the coordination geometry of the selected metal ion with different ligands can give rise to a great variety of supramolecular scaffolds for different applications[15]. The design of supramolecular entities is driven by the creation of tailored empty spaces capable of hosting guests of interest[16]. Various supramolecular metal-based structures/molecules have been explored within this area, including Metal–Organic Frameworks (MOFs) and SCCs. SCCs are discrete molecular arrangements that can exist and maintain their structure and porosity in solution[17,18]. They can act as drugs, and signaling agents for molecular recognition, or can be catalytic in performing bio-orthogonal reactions. Finally, more than one type of metal center and different functional organic moieties can be combined to generate tandem-multifunctional systems at the pinnacle of SCC design. Overall, the field of supramolecular chemistry is a rapidly growing and exciting area of research, with broad implications for a wide range of applications in various fields. The integration of these materials into biology and medicine holds the key to advancing healthcare and improving patient outcomes, with groundbreaking discoveries and innovative therapeutics on the horizon.

Schiff base ligands, known for their versatility[19], play crucial roles in biological systems, offering valuable insights into biomolecule structures and functions. Widely used in catalysis due to their ability to coordinate with metal ions and enhance reaction rates, Schiff bases serve as valuable models for understanding metalloprotein behavior[20]. Their synthetic accessibility allows for the creation of a diverse range of ligands with distinct properties[21,22], opening up possibilities in various fields, including antitumor, antimicrobial, antifungal, and anti-inflammatory applications[23–36].

In the synthesis realm, ultrasound-assisted preparation emerges as a highly effective method for crafting nanoscaled SCCs. Its adaptability to specific synthesis needs enhances its popularity in nanomaterial creation[37]. Transition metal ions and complexes, particularly those involving copper, have gained prominence in disease treatment. Chelating ligands with metal ions, especially in developing antibacterial agents, showcases their potential to enhance potency[38–40] and cellular uptake[41].

Copper structures, particularly copper complexes, have demonstrated prowess in diverse biological activities[42], ranging from DNA-binding and antioxidant studies[43] to anticancer investigations[44,45]. The ability of copper complexes to generate cytotoxic reactive oxygen species (ROS) contributes to their antiproliferative properties[46,47]. Their selective accumulation in tumors, facilitated by cancer cell membranes' permeability, underscores their potential as novel therapeutic agents[48].

The synthesis and characterization of metal complexes, particularly Cu complexes, have gained substantial attention due to their versatile applications in various scientific and biomedical fields. Despite significant advancements, there remains a need for innovative synthesis methods and comprehensive characterization of these complexes to fully harness their potential. Despite the extensive research on metal complexes, there remains a gap in the understanding of how sonochemical synthesis can influence the structural and biological properties of Cu^{2+} complexes. Traditional synthesis methods often result in longer reaction times and less control over the formation of desired complexes. Therefore, exploring sonochemical synthesis provides an opportunity to develop more efficient and controlled methods for creating Cu^{2+} complexes with potentially enhanced biological activities. This research aimed to explore a novel class of Cu^{2+} complexes synthesized through sonochemical methods, a technique known for its efficiency and ability to produce unique nanostructured materials, focusing on their structural, spectroscopic, and biological properties. The sonochemical synthesis method employed in this research offers several advantages over conventional synthesis techniques. Ultrasonic irradiation enhances the reaction kinetics, enabling rapid and efficient synthesis of the Cu^{2+} supramolecular complexes. The use of high-frequency sound waves generates localized hot spots with high temperatures and pressures, promoting the formation of these complexes in a controlled and reproducible manner. This unique supramolecular architecture, elucidated through single-crystal X-ray structure determination, offers insights into the design and development of functional materials with tailored properties. Cu^{2+} was chosen as the metal center in this study due to its unique properties and potential applications in various fields, particularly in biomedical research. Cu^{2+} complexes have demonstrated remarkable biological activities, including antioxidant and anticancer properties. The ability of Cu^{2+} complexes to generate cytotoxic ROS contributes to their antiproliferative properties, making them promising candidates for cancer treatment. In addition, their selective accumulation in tumors, facilitated by cancer cell membranes' permeability, further underscores their potential as novel therapeutic agents. Moreover, the biological evaluation of these complexes revealed remarkable antioxidant activity, low cytotoxicity on fibroblast and MCF-7 cell lines, and non-hemolytic behavior.

Experimental

Materials and methods

The reagents and chemicals employed in the present study were procured from Merck and Sigma-Aldrich and were used as received without additional purification. All calculations were conducted in the OLEX2 software kit by the use of the SHELXT and the SHELXL software for a solution and refinement, respectively[49]. For 3D images, it was done using ToposPro software version 5.5.2.2[50]. FT-IR analysis was conducted using FT-IR 4600 type A spectrophotometers. The PXRD measurements were performed using an X'pert diffractometer from

Philips with monochromated CuKα radiation (λ = 1.54056). Mercury software was employed to generate PXRD powder patterns simulated based on single-crystal X-ray data. The simulation aimed to predict the expected PXRD patterns for comparison with the experimental results. The TGA experiments were conducted using a Perkin Elmer Sta6000 apparatus, with temperature ranges spanning from 30 to 800 °C. The morphology and size distribution of two coordination complexes, (1) and (2), were characterized by SEM using a FESEM-FEI Nanosem 450 instrument. The nanostructures and dimensions of two coordination compounds, (1) and (2), were further confirmed by TEM using a TEM Philips EM208s instrument. Investigation and calculations related to cytotoxicity were done using GraphPad Prism software.

Samples preparation

Synthesis of the Cu^{2+} complexes using branch tube approach

Single crystals of Cu^{2+} complexes were synthesized using the branch tube method (Scheme S1). Typically, 1 mmol (0.199 g) of $Cu(OAc)_2{\cdot}H_2O$, 1 mmol (0.167 g) of pyridine-2,6-dicarboxylic acid (L) ligand, and 1 mmol (0.126 g) of 2,4-diamino-6-hydroxypyrimidine (L′) ligand for complex (1) and 1 mmol (0.199 g) of $Cu(OAc)_2{\cdot}H_2O$, 1 mmol (0.167 g) of pyridine-2,6-dicarboxylic acid (L) ligand, and 1 mmol (0.068 g) of imidazole (Im) ligand for complex (2) were poured in one arm of a branch tube. Then, methanol (MeOH) solvent was slowly added to fill both arms of the sealed tube. The arm containing the ligand mixture was immersed in an oil bath at 60 °C, while the other arm was kept at room temperature. After allowing the reaction to proceed for 1 day, green crystals of complex (1) and blue crystals of complex (2) were obtained in the arm and kept at room temperature. The resulting crystals were carefully collected, washed with MeOH, and dried in the air. The schematic of the as-presented approach is illustrated in Scheme S1a for complex (1) and Scheme S1b for complex (2). This method provides a straightforward approach for the preparation of single crystals of complexes with the advantage of controlled temperature conditions in the branch tube setup.

Sonochemical synthesis of Cu^{2+} complexes using ultrasonic assisted

For the synthesis of complex (1) by the sonochemical method, an aqueous solution containing $Cu(OAc)_2{\cdot}H_2O$ (20 mL, 50 mmol) was introduced into a high-density ultrasonic probe with a power output of 60 W, followed by the dropwise addition of a solution of pyridine-2,6-dicarboxylic acid (20 mL, 50 mmol) and a solution of 2,4-diamino-6-hydroxypyrimidine (20 mL, 50 mmol). Subsequently, a green precipitate was generated after 1 h incubation period. The resulting precipitates were then isolated through filtration, washed with water, and air-dried. For ultrasonic irradiation, a multiwave ultrasound generator (ultrasonic sonicator-3000; Inc, Farmingdale, NY) was employed, equipped with a converter/transducer and a titanium oscillator (horn) measuring 12.5 mm in diameter. This generator operated at a frequency of 20 kHz with a maximum output power of 600 W. For the synthesis of complex (2) by the sonochemical method, An aqueous solution containing $Cu(OAc)_2{\cdot}H_2O$ (20 mL, 50 mmol) was introduced into a high-density ultrasonic probe with a power output of 60 W, followed by the dropwise addition of a solution of pyridine-2,6-dicarboxylic acid (20 mL, 50 mmol) and a solution of imidazole (20 mL, 50 mmol). Subsequently, a blue precipitate was generated after 1 h incubation period. The resulting precipitates were then isolated through filtration, washed with water, and air-dried. For ultrasonic irradiation, a multiwave ultrasound generator (ultrasonic sonicator-3000; Inc, Farmingdale, NY) was employed, equipped with a converter/transducer and a titanium oscillator (horn) measuring 12.5 mm in diameter. This generator operated at a frequency of 20 kHz with a maximum output power of 600 W.

In vitro biological assays

Antioxidant activity

The DPPH (2,2-diphenyl-1-picrylhydrazyl) assay is a commonly used method to determine the antioxidant activity of different substances by measuring their ability to scavenge the stable DPPH radical. The objective of this study is to compare the DPPH radical scavenging activity of complexes with ascorbic acid[51]. For this, DPPH solution with constant concentration in MeOH, and solutions of complexes (1) and (2) and ascorbic acid in distilled water with concentrations ranging from 1.25–15 µg/mL were prepared. A mixture of 900 µL of DPPH solution and 100 µL of each concentration of the samples was incubated for 30 min. DPPH solution without any sample served as the blank. After incubation, the absorbance was measured at 517 nm to determine the antioxidant properties of the samples. The DPPH radical scavenging activity was quantified using the equation:

$$(\%)\ DPPH\ radical\ scavenging\ activity = \left(\frac{A_{blank} - A_{sample}}{A_{blank}}\right) \times 100 \quad (1)$$

where A_{blank} and A_{sample} are absorbances of DPPH and sample, respectively. This method ensures a detailed examination of DPPH radical scavenging activity, offering valuable insights into the antioxidant effectiveness of the compounds compared to the established antioxidant, ascorbic acid.

In a controlled environment maintained at an ice water bath temperature, a solution containing 10 mL of $NaNO_2$ (50 mM) was mixed with 10 mL of H_2O_2 (25 mM) and vigorously stirred. Subsequently, 10 mL each of HCl (1 M) and NaOH (1.5 M) were promptly added, resulting in the formation of a pale yellow solution. The molar extinction coefficient was determined by measuring the absorbance of the solution at 302 nm using UV–visible spectrophotometry, yielding a value of $1670 \pm 50\ M^{-1}\ cm^{-1}$. To assess the proxynitrite ($ONOO^-$) scavenging capability, UV–Vis absorption spectra were systematically acquired in a concentration-dependent and time-dependent manner across the spectral range of 200–500 nm. The optimal $ONOO^-$ concentration was adjusted to ensure absorption within the desired spectral range. Subsequently, varying concentrations (ranging from 0–15 µg/mL) of complexes were introduced into the $ONOO^-$ solution, and the absorbances of the respective

samples were recorded using UV–Vis spectrophotometry. IC_{50} values of complexes were determined, and their efficacy was evaluated over 30 min.

H_2O_2 is a stable molecule with notable oxidizing and reducing properties. It can create hydroxyl radicals (·OH) and act as a catalyst for radical reactions. The process is interrupted by catalase which reduces H_2O_2 to H_2O and O_2. Elevated concentrations of H_2O_2 can lead to oxidative stress, potentially causing cellular damage and cell death.

$$2H_2O_2 \rightarrow^{catalase} O_2 + 2H_2O \tag{2}$$

The complexes were subjected to investigation for their ability to scavenge H_2O_2 in a manner analogous to catalase. A solution containing complexes at a concentration of 0.5 µg/mL, along with H_2O_2 at 10 M, was prepared, resulting in the formation of bubbles indicated by the reaction. The catalase-like (CAT-like) activity of complexes was assessed by inhibiting the production of fluorescent 2-hydroxyterephthalic acid (2-HTPA) compared to the nonfluorescent terephthalic acid (TPA). This was achieved by preparing a solution containing H_2O_2 (10 mM), TPA (0.5 mM), and varying concentrations of complexes (ranging from 0–15 µg/mL) in phosphate-buffered saline (PBS) at pH 7.4. When TPA is exposed to H_2O_2, absorbs ·OH, leading to the production of fluorescent 2-HTPA with an emission peak at 425 nm (excitation wavelength: 320 nm) (Scheme S2). This experimental approach provides insights into the CAT-like activity of complexes in scavenging H_2O_2. The measurement of fluorescent 2-HTPA production, In comparison to non-fluorescent terephthalic acid, serves as a quantitative indicator of their effectiveness in neutralizing H_2O_2.

Blood compatibility (hemolysis) test

Fresh blood samples were obtained from the Kermanshah Blood Bank Center. The samples were centrifuged at 1300 rpm for 5 min to separate RBCs from plasma. Subsequently, the RBCs were diluted with PBS at a 1:9 ratio. The diluted blood was then mixed with different concentrations (ranging from 50–200 µg/mL) of complexes in microtubes and incubated for 1 h at 37 °C. The evaluation involves comparing the hemolytic activity of the compounds to negative and positive controls. 500 µL of the diluted blood was added to microtubes containing varying concentrations of complexes. PBS and distilled water, in conjunction with blood, served as the negative (0% lysis) and positive control (100% lysis), respectively. The 1-h incubation period at 37 °C provided for the interaction between the complexes and RBCs. Following incubation, the microtubes were centrifuged, and the supernatant was transferred to a 96-well plate. Hemoglobin release, indicating damaged RBCs, was measured at 545 nm using an enzyme-linked immunosorbent assay (ELISA) reader. The hemolytic index was calculated using the following formula:[52]

$$(\%)\ \ Hemolysis = \left(\frac{A_{sample} - A_{NC}}{A_{PC} - A_{NC}}\right) \times 100 \tag{3}$$

where A_{Sample}, A_{NC}, and A_{PC} are the absorbances of the sample, negative control, and positive control, respectively. To ensure reliability, three duplications were performed for each sample. The hemolysis test offers crucial insights into the potential damage caused to RBCs by complexes. The hemolytic index calculation allows for a quantitative assessment of the hemolytic activity of the complexes, indicating their blood compatibility. This information is vital for evaluating the safety and biocompatibility of these complexes for potential biomedical applications.

MTT assay

The MTT (3-(4,5-dimethylthiazol-2-yl)-2,5-diphenyltetrazolium bromide) assay is a colorimetric method used to assess the viability and cytotoxicity of cells when exposed to various compounds. MCF-7 breast cancer and fibroblast cell lines were obtained from the National Center of Genetic and Biological Resources of Iran. Frozen MCF-7 and fibroblast cell lines were thawed, and then introduced into preheated Dulbecco's Modified Eagle Medium (DMEM) in a Falcon tube. The cells were cultured in DMEM supplemented with fetal bovine serum (FBS), penicillin, and streptomycin. Upon reaching 70% confluency, the cells were washed, treated with trypsin, and centrifuged. The MTT assay was employed to assess cell viability after incubation with varying concentrations of complexes. The cells were cultured in a 96-well plate and treated with different concentrations of complexes and cisplatin as positive control for a 24-h incubation period. Following this, The MTT solution was added, and further incubation allowed mitochondrial dehydrogenase to reduce MTT to blue formazan material[53]. Formazan crystals were dissolved, and cell viability was measured at 570 nm using an ELISA reader. Cell viability was calculated using the following formula:[54]

$$(\%)\ \ Cell\ viability = \left(\frac{A_{sample}}{A_{control}}\right) \times 100 \tag{4}$$

where A_{sample} and $A_{control}$ represent the absorbances of the sample and control, respectively. IC_{50} values, indicating the concentration causing 50% proliferation inhibition in each cell line, were determined using nonlinear regression, considering the mean of three replications. This approach, employing the MTT method, allowed for a thorough assessment of cell viability in MCF-7 and fibroblast cell lines treated with complexes. The determination of IC_{50} values offers valuable insights into the potential inhibitory effects of these complexes on cell proliferation, thereby contributing to their characterization for potential therapeutic applications.

Antibacterial activity

The antibacterial properties of complexes were investigated using the Broth Dilution Method on standard strains of *S. aureus* (Gram-positive) and *E. coli* (Gram-negative). Initially, a bacterial suspension was prepared to achieve turbidity equivalent to the standard McFarland 0.5, corresponding to 1.58×10^8 colony-forming units per milliliter (cfu/mL). For the Broth Dilution method, successive dilutions of complexes were prepared at concentrations of 2000, 1000, 500, 250, 125, 62.5, and 31.25 µg/mL, using the dilution method. These dilutions were combined with the bacterial suspension to create a series of mixtures. Subsequently, the bacterial and complexes mixtures were incubated at 37 °C for 24 h to simulate conditions conducive to bacterial growth. Following this incubation period, the turbidity resulting from bacterial growth was assessed. The well exhibiting no turbidity, indicating inhibition of bacterial growth, was identified as the Minimum Inhibitory Concentration (MIC). Furthermore, the Minimum Bactericidal Concentration (MBC) was determined as the lowest concentration capable of eradicating the bacteria. This experimental design using the Broth Dilution Method enables the evaluation of the antibacterial properties of complexes against both Gram-positive and Gram-negative bacterial strains. The determination of MIC and MBC values offers insights into the effectiveness of these substances in inhibiting and eradicating bacterial growth, thereby contributing to their potential application as antibacterial agents. In the disc diffusion method, Mueller Hinton Agar specific culture medium was used for the cultivation of microorganisms. Initially, the microorganisms were pre-cultured in their respective media for 24 h at 37 °C. Subsequently, a suspension of each bacterium (equivalent to 0.5 McFarland standard) was evenly spread across the surface of the culture medium plate using a sterile swab. 50 µl of complex solutions, at concentrations of 1.5 and 2 mg/mL, were applied to separate discs, which were then evenly spaced on the inoculated plates. After an incubation period of 24 h at 37 °C, the diameters of the inhibition zones were measured using a caliper and recorded. Standard antibiotic discs containing gentamicin were used as positive controls.

Results and discussion

Crystal and molecular structure

Characterization of crystal structures of complexes

The structural confirmation of complex (1) was accomplished through single-crystal X-ray structure determination, employing X-ray crystallography to elucidate its solid-state structure. Complex (1) was recognized as a 0D supramolecule (Table S1), exhibiting a monoclinic crystal system and the *C2/c* space group. Within the asymmetric unit, complex (1) includes components of Cu^{2+}, L, L′, and H_2O molecule. Figure 1a illustrates the molecular coordination around the Cu^{2+} ion. The Cu^{2+} ion is coordinated by two nitrogen atoms from the L and L′ ligands [Cu1–N1 = 2.008 and Cu1–N2 = 2.047 Å], two oxygen atoms from the L ligand [Cu1–O1 = 2.340 and Cu1–O2 = 2.340 Å], and two oxygen atoms from H_2O molecule [Cu1–O3 = 2.020 and Cu1–O4 = 2.020 Å] (Table S2). This coordination arrangement results in a distorted octahedral geometry for the complex (1) (Fig. 1c), with the angles around the Cu^{2+} center falling within the range of 75.11°–104.99°. Due to crystallographic C_2 rotation axes, only half of the complex is crystallographically independent. The C_2 symmetry induces disorder in the diaminopyrimidine molecule, exhibiting a 0.5 occupation factor for the two components. Despite the near-perfect overlap of equivalent atoms, N–H and C–H bonds ortho to the keto group display some deviation. The crystal structure is (statistically) centrosymmetric in the *C2/c* space group. The equatorial ligands exhibit a dihedral angle of 10.1(1)°, indicating their non-coplanar arrangement. In the crystal, the molecules form planar layers through both strong and weak hydrogen-bonding interactions (Fig. S1). Ring patterns $R_4^2(8)$ and $R_2^2(8)$ are observed within these layers (Fig. S2). Similarly, complex (2) underwent structural confirmation via single-crystal X-ray structure determination, revealing its status as a 0D supermolecule. Complex (2) crystallizes

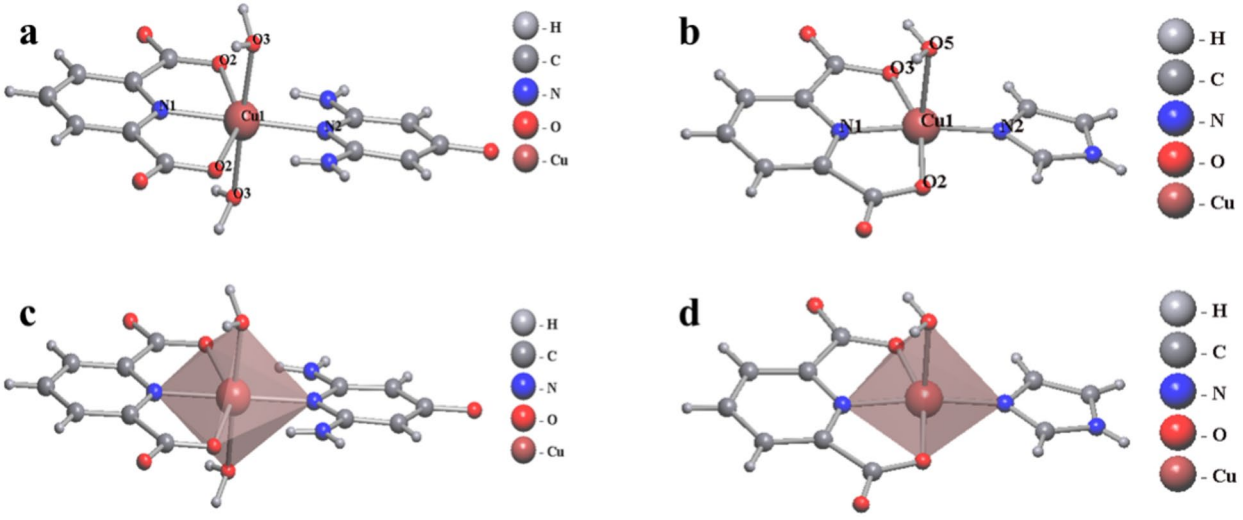

Fig. 1. X-ray molecular structures of complexes (1) (**a**) and (2) (**b**), the coordination environment of Cu^{2+} cation in complexes (1) (**c**) and (2) (**d**).

within the triclinic crystal system with the *P*-1 space group. The asymmetric unit comprises one Cu^{2+} center, one L ligand, one Im ligand, and one H_2O molecule. Figure 1b illustrates the molecular coordination around the Cu^{2+} ion. The Cu^{2+} ion is coordinated by two nitrogen atoms from the L and Im ligands [Cu1–N1 = 1.897(2) and Cu1–N2 = 1.919(2) Å], two oxygen atoms from the L ligand [Cu1–O2 = 2.031(2) and Cu1–O3 = 2.021 Å], and one oxygen atom from a H_2O molecule [Cu1–O1 = 2.361(2) Å] (Table S3). This coordination arrangement results in a distorted square pyramid geometry for the complex (2) (Fig. 1d) with the angles around the Cu^{2+} center falling within the range of 80.43–99.58°. The imidazole and pyridine-6-dicarboxylate ligands exhibit a dihedral angle of 10.05(12)°, indicating their non-coplanar arrangement. In the crystal, the molecules are organized into planar layers through strong and weak hydrogen-bonding interactions. Notably, ring patterns $R_4^2(10)$ are observed within these layers, as shown in Fig. S3, which are parallel to the lattice planes [1-1-3]. The stacking distances between the planes measure 3.152 Å. Selected bond lengths are provided in Table S3. These detailed structural insights provide a thorough understanding of the coordination geometries, symmetry elements, and crystallographic arrangements of the complexes. The centrosymmetric nature and hydrogen-bonding patterns observed in the crystal structures contribute to the broader knowledge of Cu^{2+} supramolecular complexes.

Intermolecular interactions in solid state of complexes

Complex (1) showcases a sturdy molecular framework, where the monomer complex is constructed through robust bonds. The supramolecular assembly is extended through weak interactions, contributing to the overall 0D structure. Van der Waals bonds connect complex (1) monomers, contributing to the supramolecular assembly. Hydrogen bonding interactions are notable within the 0D structure. These interactions involve the H atom of the NH_2 group in the L′ ligand and the O atom of $–COO^-$ groups in the L ligand. In addition, hydrogen bonding occurs between the H atoms of H_2O and the O atoms of $–COO^-$ groups in the L ligand (Fig. S4a). Similarly, complex (2) presents notable intermolecular interactions contributing to its 0D structure. Hydrogen bonding interactions are observed, particularly between the H atom of the H_2O and the O atoms of $–COO^-$ groups in the L ligand (Fig. S4b). Detailed data on selected hydrogen bond lengths in both complexes are furnished in Table S4, delineating the precise distances associated with these interactions. In both complexes, π–π interactions between aromatic rings contribute to the stability of the crystal structure. The π–π interactions between aromatic rings for complexes (1) and (2) are shown in Fig. S5a and S5b, respectively. The distance between two aromatic rings measures 3.863 Å in complex (1) (Fig. S6a) and 3.660 Å in complex (2) (Fig. S6b).

Hirshfeld surfaces analysis

The intermolecular interactions and crystal architectures of two coordination complexes were scrutinized utilizing Hirshfeld surface analysis alongside two-dimensional fingerprint plots via the Crystal Explorer 3.0 software[55]. Hirshfeld surface analysis is a pioneering technique for visualizing and quantifying the intricacies and extent of intermolecular contacts within molecular crystals[55]. The Hirshfeld surface is defined as the boundary between a molecule and its environment in the crystal, where the environment includes all other molecules and the void space. The surface is constructed by partitioning the crystal's electron density into molecular contributions using the stockholder scheme[56]. The surface can be visually encoded with various properties that denote the nature and intensity of intermolecular interactions, such as the distance to the nearest nucleus inside (d_i) and outside (d_e) the surface, electrostatic potential, shape index, and curvature. The 2D fingerprint plots are derived from the Hirshfeld surface, plotting the d_i and d_e values for each point on the surface into a scatter plot. These plots afford a graphical representation of the relative contributions of disparate contact types to the Hirshfeld surface, encompassing hydrogen bonds, van der Waals interactions, and π–π stacking. The 3D Hirshfeld surfaces for complexes were constructed with a volume of 363.34 $Å^3$ and an area of 339.81 $Å^2$, respectively, and colored by the normalized contact distance (d_{norm}), which is defined as $d_{norm} = (d_i + d_e)/\langle d_i + d_e \rangle$, where $\langle d_i + d_e \rangle$ is the mean value of $d_i + d_e$ over the entire surface. The d_{norm} values range from 0.639 au (blue) to 1.193 au (red) on the color scale, where blue indicates regions of close contact and red indicates open space regions[57]. The 3D Hirshfeld surfaces for complexes (1) and (2) are shown in Fig. 2a,b, respectively.

The Hirshfeld surfaces for complexes were mapped according to d_{norm} (Fig. S7a and S7f), d_i (Fig. S7b and S7g), d_e (Fig. S7c and S7h), shape index (Fig. S7d and S7i), and curvature (Fig. S7e and S7j). In both complexes, the predominant contributions emanate from H…H, O…H, C…C, and C…H contacts, indicative of van der Waals interactions and hydrogen bonds. The lattices are stabilized by both hydrogen bonds and dispersion forces. The contribution of intermolecular interactions for complexes (1) and (2) are shown in Fig. S8a and S8b, respectively. The contribution of intermolecular interactions from the results of Hirshfeld surface analysis is as follows: In both complexes, intermolecular interactions were obtained from the highest share to the lowest share. According to the diagrams shown in Fig. S9, the trends of intermolecular interactions are as follows: (H…H > O…H > C…C > C…H > N…H > N…C > C…O > H…C > O…C > O…O > N…O > O…N > N…N for complex (1) (Fig. S9a) and H…H > O…H > C…H > C…C > C…O > N…H > O…O > N…O > N…N > Cu…O for complex (2) (Fig. S9b). The high contribution of H…H and O…H contacts in both complexes is attributed to the presence of carboxylic acid groups and water molecules within the structures, forming robust hydrogen bonds with each other and with neighboring molecules. The contribution of H…H and O…H contacts in complex (1) is slightly higher than in complex (2) due to the presence of NH_2 and OH groups on the pyrimidine ligand, which also form hydrogen bonds with the environment. Hirshfeld surface analysis and the associated 2D fingerprint plots provide a comprehensive and unbiased perspective of the intermolecular interactions and crystal packing of both complexes, revealing the similarities and distinctions between the two compounds. The analysis shows that both compounds have compact and flat molecular shapes with formidable hydrogen bonds and feeble van der Waals interactions with the environment. The analysis also shows that the main difference between the two

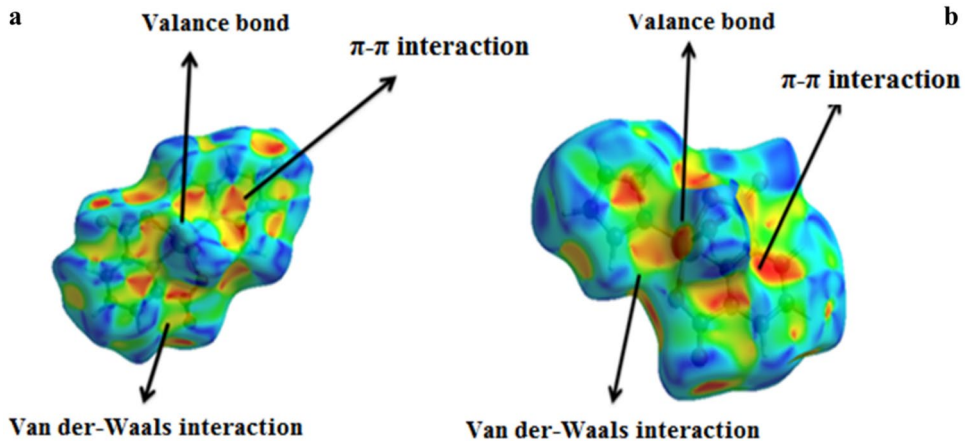

Fig. 2. Hirshfeld surface of complexes (1) (**a**) and (2) (**b**). The image was generated using ToposPro software version 5.5.2.2. The software is available at https://topospro.com[50].

complexes is the presence of the pyrimidine ligand in complex (1), which introduces additional hydrogen bonds and modifies the shape and size of the molecule and the void space.

Spectroscopic analysis

FT-IR spectral studies

The FT-IR spectra of complexes in Fig. 3 exhibit distinctive absorption bands, providing insights into the vibrational characteristics of the ligands and metal–ligand interactions. In the FT-IR spectrum in complex (1), the N–H and NH_2 groups display characteristic stretching vibrations in the range of 3400 cm^{-1} which are related to pyridine-2,6-dicarboxylic acid and 2,4-diamino-6-hydroxypyrimidine ligands. The observed absorbance band at 1430 cm^{-1} corresponds to stretching vibrations of C=C bonds in the aromatic ring, which further characterizes the structure of the ligands. In addition, an absorption band was demonstrated at approximately 1600 cm^{-1}, indicating stretching vibrations of the C=N group in the pyrimidine ligand. Weak peaks at 594 cm^{-1} and 436 cm^{-1} indicate stretching vibrations of the Cu–N and Cu–O bonds, respectively, providing insights into the coordination environment of the Cu^{2+} center in the complex. For complex (2), the N–H group exhibits characteristic stretching vibrations around 3400 cm^{-1} related to pyridine-2,6-dicarboxylic acid and imidazole ligands. An absorption band at approximately 3100 cm^{-1} signifies the presence of C–H bonds in the aromatic rings of the pyridine-2,6-dicarboxylic acid and imidazole ligands. Absorbance peaks at 1430 cm^{-1} denote stretching vibrations of C=C bonds in the ligands. An absorption band at 737 cm^{-1} suggests the presence of a coordinated H_2O

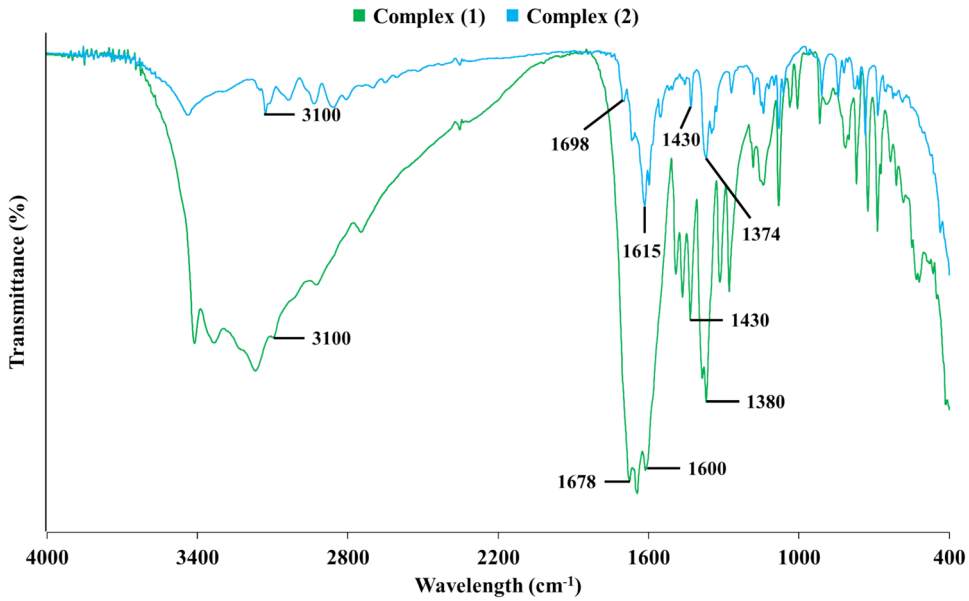

Fig. 3. FT-IR spectra of complexes (1) and (2).

within the structure of the complex. Weak peaks at 548 cm^{-1} and 464 cm^{-1} respectively correspond to stretching vibrations of the Cu–N and Cu–O bonds, providing information about the coordination bonds in the Cu^{2+} complex[58–61]. In the FT-IR spectrum in complex (1), two bands were observed at 1380 and 1678 cm^{-1} that arise from the symmetric and asymmetric stretching of the carboxylate groups (ν_s and ν_{as}, respectively). The difference (Δ_{as-s}) between these two bands is 298 cm^{-1}, suggesting a monodentate mode. In complex (2), the $\Delta\nu$ ($\nu_s = 1374$ and $\nu_{as} = 1698$) of 324 cm^{-1} is larger than Δvion (ca. 165 cm^{-1}) and should be attributed to monodentate coordination[62]. FT-IR analysis furnishes valuable molecular-level insights into the bonding interactions and structural characteristics of complexes, aiding in a comprehensive understanding of their chemical composition and coordination environments.

PXRD spectral studies

PXRD analysis was carried out to compare the simulated patterns from single-crystal X-ray data with the experimental PXRD patterns of complexes. The PXRD patterns in Fig. 4a,b illustrate a comparison between the simulated patterns generated from single-crystal X-ray data and the experimental PXRD patterns obtained through the sonochemical process for complexes (1) and (b), respectively. This comparison shows satisfactory matches between the simulated and experimental powder X-ray diffraction patterns for both complexes, indicating a high level of consistency between the nanostructured compounds produced through sonochemical synthesis and those obtained via conventional single-crystal evaporation. The observed peak characteristics provide insights into the particle size and crystal lattice regularity. Wider peaks indicate nanometer-sized particles, while sharper peaks suggest a more regular crystal lattice. Despite variations in peak width, the PXRD data indicates that crystal and nano-structure compounds share the same phase. This observation reinforces that the compounds obtained via sonochemical synthesis are identical to those obtained through conventional single-crystal evaporation. PXRD analysis serves as a robust tool for confirming the phase identity, crystal structure regularity, and particle size of complexes synthesized via the sonochemical process. The consistency observed between simulated and experimental patterns validates the reliability of the sonochemical method for producing nano-structured compounds with characteristics similar to those obtained through traditional single-crystal methods.

Thermogravimetric analysis

TGA was utilized to evaluate the thermal stability of complexes. Figure 5 illustrates the thermal behavior of complexes. The analysis reveals distinct weight-loss events corresponding to specific temperature ranges. A weight loss of 9.00% is observed for complex (1), attributed to the removal of two water molecules (calculated value: 9.17%). The compound remains stable up to 250 °C. The second weight-loss event, accounting for 33.00% of the weight, is associated with the loss of the L′ ligand (calculated: 32.20%). The third weight-loss event in this temperature range (32.40%) is linked to the loss of L ligand, except for two hydroxyl groups of the ligand (calculated: 33.39%). The remaining 24.78% matches with the $Cu(OH)_2$ group (calculated: 24.82%). Continued heating results in the removal of water molecules, leaving copper oxide (CuO) as a stable species (Fig. 5a). Complex (2) shows distinct thermal behavior and weight loss events. A weight-loss of 53.30% is observed, corresponding to the loss of L ligand (calculated: 53.02%). A subsequent weight-loss event (26.29%) aligns with the removal of Im ligand and water groups (calculated: 27.23%). Continued heating leads to the removal of water molecules, resulting in copper oxide (CuO) as the stable species (Fig. 5b). TGA analysis provides a comprehensive understanding of the thermal decomposition behavior of complexes. The observed weight loss events and their corresponding temperatures offer insights into the stability and decomposition processes, aiding in the characterization of these compounds under varying thermal conditions.

SEM and EDS analysis

The SEM images of complexes (1) and (2) are depicted in Fig. 6a,b, respectively. The SEM images reveal that complexes (1) and (2) form rod-shaped and hexagonal-shaped particles, respectively, with a heterogeneous size distribution ranging from a few nanometers to several micrometers. The particles are relatively monodisperse in terms of their shape, aspect ratio, and orientation. The average diameter of the nanoparticles in complex (1) and the average edge length of the nanoparticles in complex (2), calculated using Eq. (5), were found to be

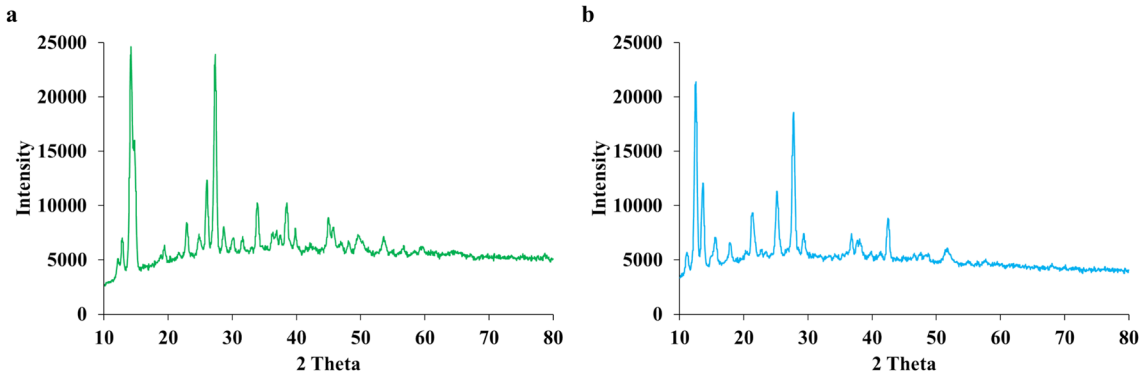

Fig. 4. PXRD patterns of single-crystal X-ray of complexes (1) (**a**) and (2) (**b**) obtained by ultrasonication.

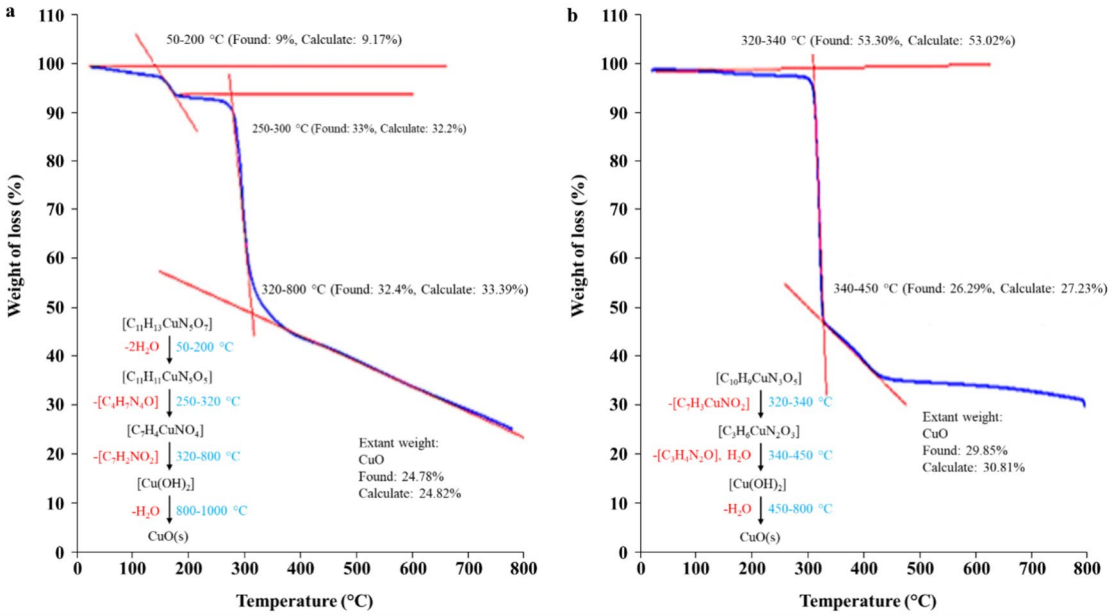

Fig. 5. Thermal behavior of complexes (1) (**a**) and (2) (**b**).

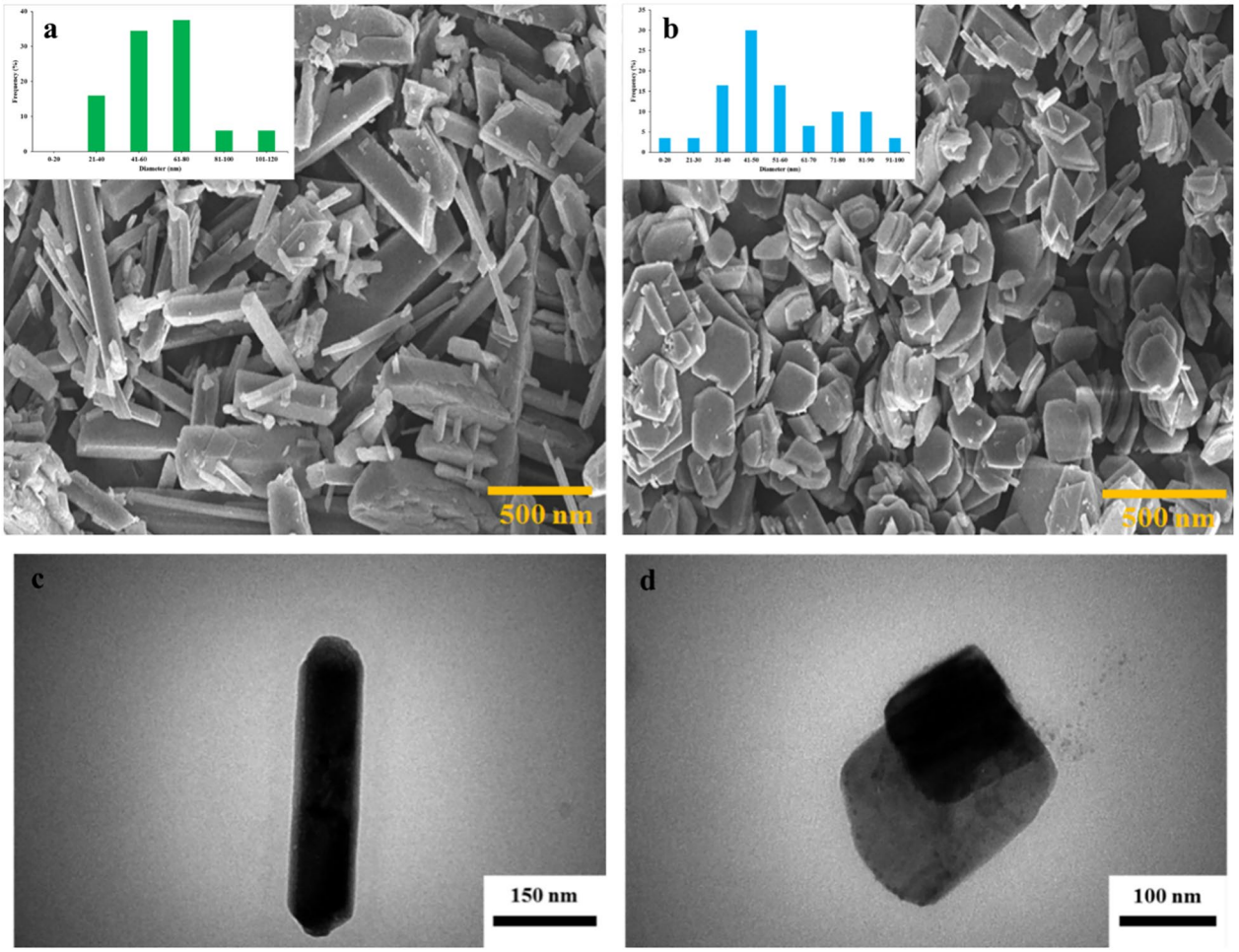

Fig. 6. SEM images of complexes (1) (**a**) and (2) (**b**), TEM images of complexes (1) (**c**) and (2) (**d**).

60–80 nm and 40–50 nm, respectively. SEM analysis offers invaluable insights into the size distribution, structural features, and overall morphology of the nanoparticles in both complexes. The observed shapes, dimensions, and monodispersed characteristics contribute to a comprehensive understanding of the nanostructures, facilitating further exploration of their properties and potential applications.

$$(\%)\ \ average\ particle\ size = \frac{Number\ of\ particles\ in\ a\ specified\ range}{The\ total\ number\ of\ particles\ measured} * 100 \quad (5)$$

EDS was employed to ascertain the chemical composition of both complexes, aiming to substantiate the structural observations. As depicted in Fig. S10a and S10b, the EDS analysis of both complexes confirmed the presence of Cu, O, N, and C elements within the structure. The close agreement between the found and calculated percentages in the EDS results affirms the reliability of the elemental composition analysis for both complexes. These findings provide robust support for the observed structures of the compounds, reinforcing the accuracy of the experimental outcomes.

TEM analysis

The TEM images of complexes (1) and (2) are shown in Fig. 6c,d, respectively. The TEM images reveal that complex (1) forms hexagonal-rod-shaped nanoparticles, while complex (2) forms square-shaped nanoparticles, both exhibiting a uniform size and shape distribution. The average dimensions of the nanoparticles were measured, revealing complex (1) to have a length and width of 430 nm and 95 nm, respectively, while complex (2) has an edge length of 125 nm. The TEM images provide a comparative assessment of the morphologies between complexes (1) and (2). The distinct geometric shapes, regularity, and uniform dimensions of the nanoparticles in both compounds are highlighted, contributing to an in-depth comprehension of their nanoscale attributes. TEM analysis serves as a valuable technique for elucidating the nanoscale characteristics, confirming the shapes and sizes of nanoparticles in both complexes. These findings contribute to a nuanced understanding of the materials, paving the way for further exploration and applications in diverse fields.

Biological activities

Antioxidant activity. DPPH scavenging

The DPPH radical, a dark purple compound with an absorption peak at 517 nm, undergoes a color change to pale yellow or colorless when reduced by a hydrogen atom or electron donor[63]. This color change can be quantified using spectrophotometry, where the degree of discoloration reflects the antioxidant potential of the substances being tested[64]. In this study, the antioxidant activities of two synthesized complexes were evaluated using the DPPH assay, with ascorbic acid included as a positive control. The results, depicted in Fig. 7, illustrate the percentage of DPPH radical scavenged by each substance across various concentrations. Complex (1) demonstrated significant antioxidant activity, whereas complex (2) exhibited none. At the highest concentration tested (15 µg/mL), complex (1) scavenged 64.72% of the DPPH radical, with an IC_{50} value of 10.67 µg/mL. The IC_{50} value, which denotes the concentration required to inhibit 50% of the DPPH radical[65], was 12.467 µg/mL for ascorbic acid, which scavenged 64.15% of the DPPH radical at the same concentration. The UV–visible absorbance spectra illustrating the DPPH scavenging activity at various concentrations of complexes (1) and (2) as well as ascorbic acid are presented in Fig. 7a–c, respectively. Additionally, Fig. 7d illustrates the outcomes of the DPPH scavenging activity.

The antioxidant activity of complex (1) and ascorbic acid was examined by measuring their time-dependent inhibition of the DPPH radical. Figure 8 illustrates the percentage of DPPH radical scavenged by each substance at a fixed concentration over time. As previously mentioned, complex (2) exhibits no antioxidant activity (Fig. 8b). Ascorbic acid rapidly and completely inhibited the DPPH radical (Fig. 8c). In contrast, complex (1) exhibited a slower and more gradual inhibition (Fig. 8a), reaching 50% scavenging after 37.29 min. This indicates that complex (1) has a different action mechanism than ascorbic acid, possibly involving a delayed or sequential electron transfer[66–68]. The time-dependent DPPH scavenging percentage is shown in Fig. 8d. The DPPH assay is a valuable tool for evaluating the antioxidant activity of various substances, as it provides a simple and reliable measure of their radical scavenging capacity[64,69]. The antioxidant activity of a substance reflects its ability to protect biological systems from oxidative stress, which results from an imbalance between the production and elimination of ROS[70]. ROS can damage cellular components such as lipids, proteins, and DNA, leading to various diseases and aging[71,72]. Antioxidants can prevent or repair the damage caused by ROS by donating a hydrogen atom or an electron to neutralize them[73]. Therefore, antioxidants are crucial in maintaining the physiological redox balance and enhancing overall well-being[74,75]. This study demonstrated that complex (1) possesses significant antioxidant activity, comparable to that of ascorbic acid, while complex (2) lacks such activity. Additionally, complex (1) showed a different kinetic behavior than ascorbic acid, suggesting a distinct mechanism of action.

Peroxynitrite scavenging

The formation of $ONOO^-$ under inflammatory conditions has significant implications for cellular function and overall health. This reactive nitrogen species (RNS) is produced through the interaction of superoxide and nitric oxide radicals, which are generated by cells during inflammation. The consequences of peroxynitrite formation are extensive, including DNA damage, activation of poly-ADP-ribose polymerase (PARP), and nitration and S-nitrosylation of proteins and lipids[76].

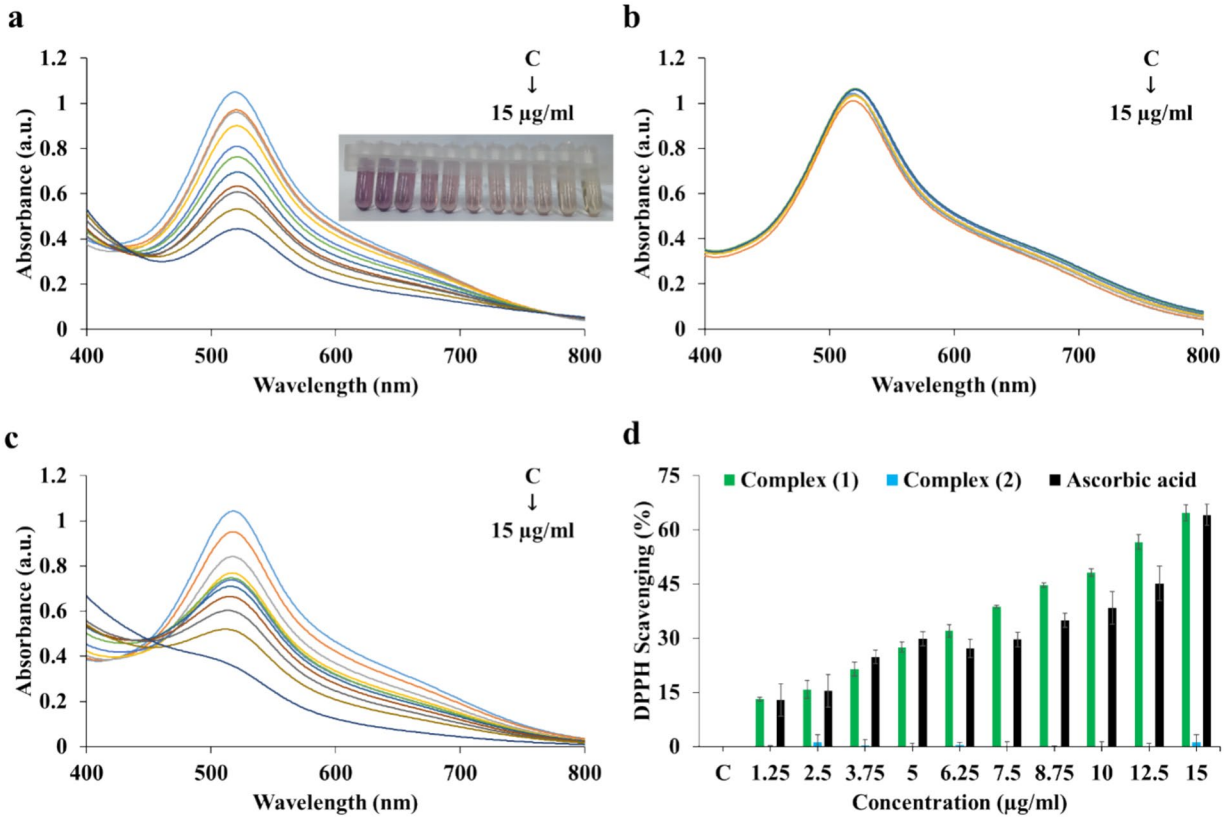

Fig. 7. UV–vis absorbance spectra of DPPH scavenging at different concentrations of complex (1) (**a**), complex (2) (**b**), and ascorbic acid (**c**). Results of DPPH scavenging activity (concentration-dependent) (**d**).

$$2O_2^{\cdot-} + NO^{\cdot} \xrightarrow{peroxynitrite} ONOO^- \quad (6)$$

One notable characteristic of $ONOO^-$ is its potent oxidizing properties. It readily converts to peroxynitrogen acid (ONOOH) by absorbing hydrogen from its surroundings, with a pKa value of 6.5–6.8. This conversion is influenced by both concentration and time. In the presence of both complexes, the absorption peak of $ONOO^-$ at 302 nm diminishes significantly as concentration and time increase, as shown in Figs. 9 and 10, respectively. The IC_{50} values for complexes (1) and (2) in the concentration-dependent state are 7.38 and 5.74 µg/mL, respectively. Similarly, in the time-dependent state, the IC_{50} values for complexes (1) and (2) are 7.17 and 3.83 min, respectively. Data in Fig. 9 indicate that under the same conditions, complex (2) exhibits a higher percentage of $ONOO^-$ scavenging compared to complex (1).

Furthermore, the diagrams in Fig. 10 support that complex (2) possesses superior $ONOO^-$ scavenging over time compared to complex (1). The UV–visible absorbance spectra at different concentrations of complexes (1) and (2) illustrating $ONOO^-$ scavenging activity are presented in Fig. 9a,b, respectively. Furthermore, the time-dependent data is depicted in Fig. 10a,b, respectively. The concentration- and time-dependent $ONOO^-$ scavenging activity results are illustrated in Figs. 9c and 10c, respectively. These findings highlight the potential of complexes as an effective antioxidant agent, which could have significant implications for combating oxidative stress and associated pathologies. In summary, the generation of peroxynitrite under inflammatory conditions can cause various cellular alterations and damage. Characterizing both complexes concerning their antioxidant properties offers valuable insights into their potential therapeutic applications. Further research and exploration of these compounds may lead to the development of novel strategies for managing oxidative stress-related disorders and improving overall health outcomes.

CAT-like activity

The results presented in Fig. 11 demonstrate the significant catalase-mimetic (CAT-mimetic) activity of both complexes. These complexes catalyze the decomposition of H_2O_2 into molecular O_2 and H_2O, as indicated by the formation of bubbles in the solution. This bubbling is characteristic of catalase, an enzyme that protects cells from oxidative damage by breaking down H_2O_2. The comparison between complexes shows that complex (1) exhibits higher catalytic efficiency than complex (2), as evidenced by the larger amount of bubbles produced. This suggests that complex (1) has a higher affinity for H_2O_2 and/or a faster turnover rate than complex (2). The samples were prepared under identical experimental conditions, eliminating any external factors that could influence the catalytic performance of the compounds. To elucidate the mechanism of the CAT-mimetic activity, the researchers studied the formation of 2-HTPA, a fluorescent product. This product is formed from the reaction of

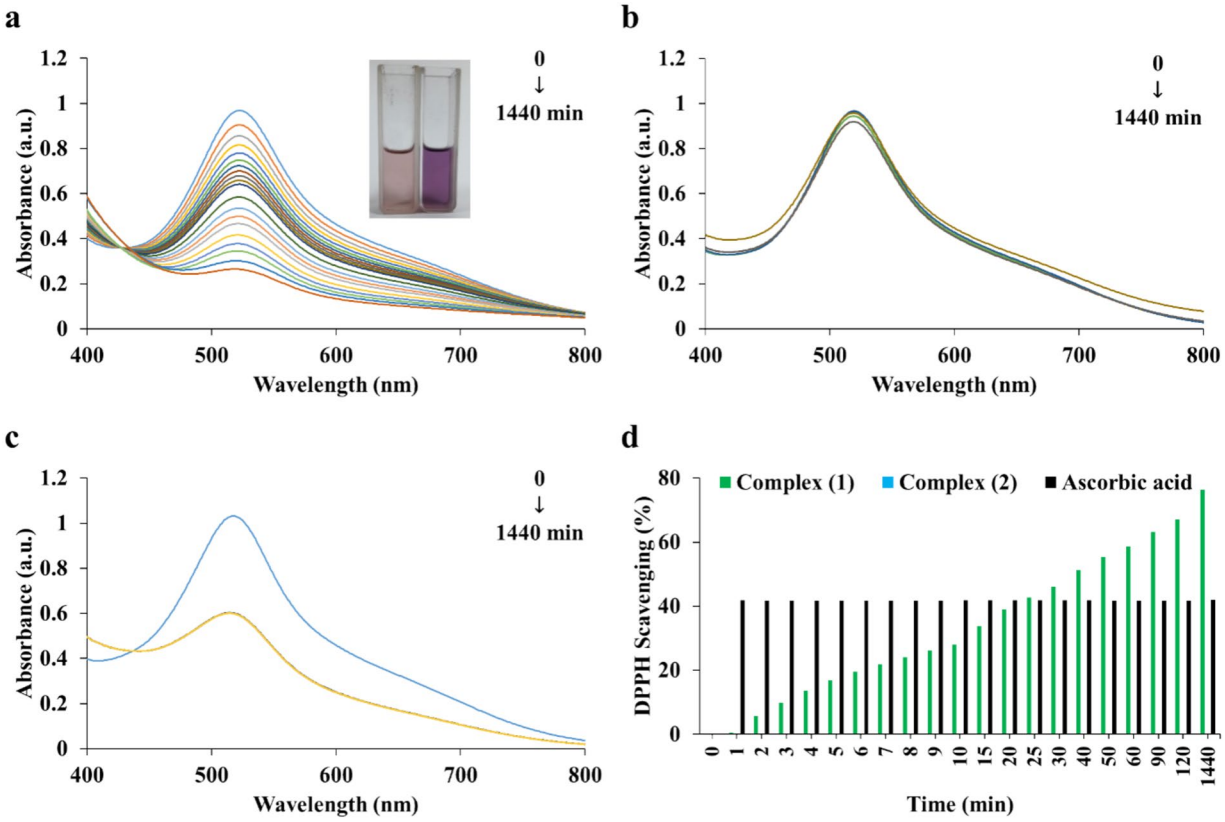

Fig. 8. UV–vis absorbance spectra of DPPH scavenging at different times of complex (1) (**a**), complex (2) (**b**), and ascorbic acid (**c**). Results of DPPH scavenging activity (time-dependent) (**d**).

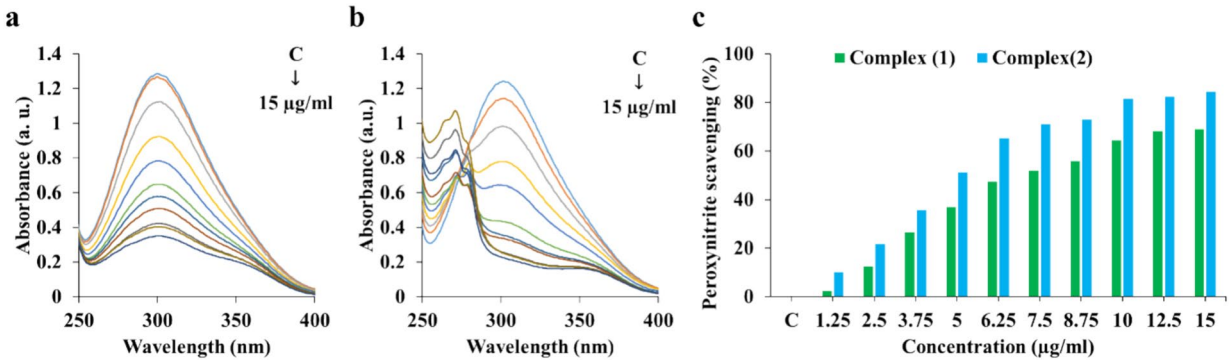

Fig. 9. UV–vis absorbance spectra of $ONOO^-$ scavenging at different concentrations of complexes (1) (**a**) and (2) (**b**). Results of $ONOO^-$ scavenging activity (concentration-dependent) (**c**).

TPA, a non-fluorescent substrate, and ·OH, a highly reactive species generated from the decomposition of H_2O_2. Complexes (1) and (2) act as catalysts in this process, facilitating the cleavage of the O–O bond in H_2O_2 and the subsequent formation of ·OH. To assess CAT-mimetic activity, fluorescence intensity is measured at 425 nm, corresponding to the emission wavelength of 2-HTPA. The fluorescence intensity is very low in the absence of complexes (1) and (2), implying that the production of ·OH is negligible without the catalysts. In contrast, the fluorescence intensity increases significantly with the addition of complexes (1) and (2), indicating that these catalysts enhance the generation of ·OH and, consequently, the formation of 2-HTPA (Fig. 11a,b). Based on these results, it can be inferred that the presence and increased concentration of complexes (1) and (2) lead to a significant enhancement in fluorescence intensity, ·OH-scavenging, and CAT-mimetic activity (Fig. 11c). These findings confirm the CAT-mimetic behavior of these compounds and suggest their potential application in the removal of H_2O_2 from biological or environmental systems.

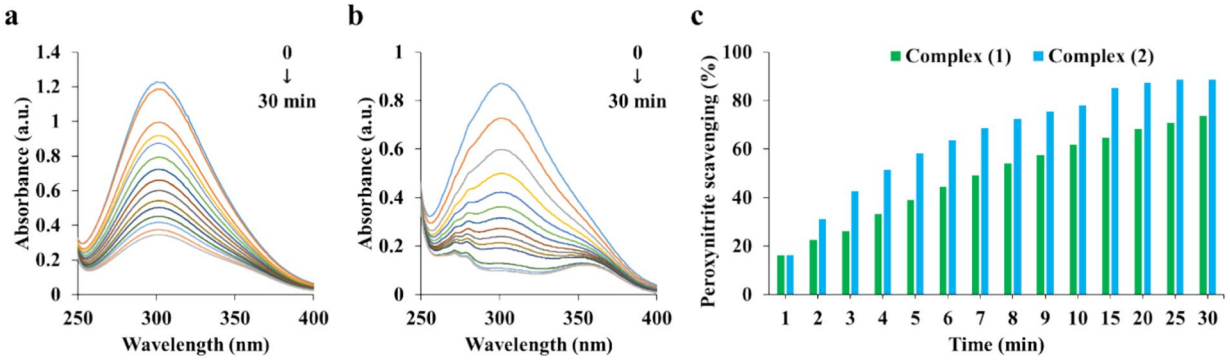

Fig. 10. UV–vis absorbance spectra of $ONOO^-$ at different times of complexes (1) (**a**) and (2) (**b**). Results of $ONOO^-$ scavenging activity (time-dependent) (**c**).

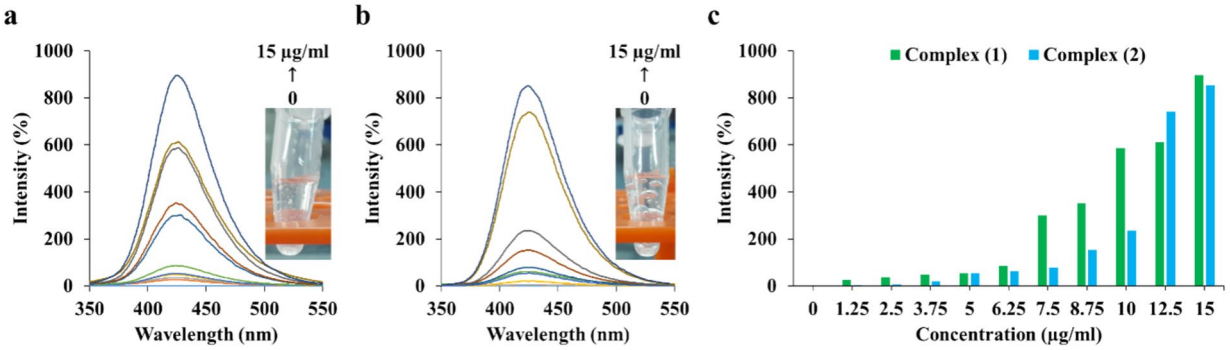

Fig. 11. Fluorescence spectra of complexes (1) (**a**) and (2) (**b**). Comparison of CAT-like activity of complexes (1) and (2) in H_2O_2 decomposition (**c**).

Blood compatibility (hemolysis)

The interaction of substances with blood can instigate inflammatory responses such as thrombosis and infection, thus compromising their biocompatibility[77]. Consequently, evaluating the hemocompatibility of any substance intended for biomedical applications is imperative. Hemolysis, defined as the disintegration of RBCs leading to the release of their contents into plasma, serves as a crucial parameter in this assessment. Hemolysis can precipitate anemia, jaundice, and renal damage, among other complications[78]. The extent of hemolysis is quantified by measuring the percentage of hemoglobin released into plasma from RBCs. As per the ASTM F756-00 (2000) standard, a substance is categorized as non-hemolytic if the hemolysis percentage is below 2%, mildly hemolytic if the percentage ranges from 2 to 5%, and hemolytic if the percentage exceeds 5%[79]. Complexes (1) and (2) manifest non-hemolytic behavior, as indicated by their hemolysis percentages being below 2%, as depicted in Fig. 12. This indicates that these compounds do not inflict significant damage upon RBCs and are compatible with blood. Moreover, the blood coagulation indices, such as prothrombin time (PT), activated partial thromboplastin time (APTT), and thrombin time (TT), also support the blood compatibility of these compounds[77]. These indices gauge the time requisite for blood to clot in the presence of various factors and reagents. The findings reveal that the coagulation times of blood samples containing complexes (1) and (2) are comparable to those of the control samples, suggesting that these compounds do not disrupt the normal coagulation process. These results elucidate the safety and compatibility of both complexes with blood, underscoring their suitability and reliability for diverse biomedical applications. Nevertheless, it is pivotal to acknowledge that these findings are preliminary, and further testing and evaluation may be essential before these compounds can be utilized in clinical settings. In summary, this research furnishes invaluable insights into the biocompatibility of both complexes, accentuating the necessity of rigorous testing to ensure the safety and efficacy of biomedical materials.

MTT assay

The cytotoxic activities of complexes (1) and (2) were evaluated using the MTT assay, a colorimetric method that measures the metabolic activity of living cells. This assay relies on the reduction of the yellow tetrazolium salt MTT to a purple formazan product by mitochondrial dehydrogenases in viable cells. The amount of formazan produced correlates with the number of living cells and is quantified by measuring absorbance at 570 nm. This assay was conducted on normal fibroblast and MCF-7 cancer cell lines, commonly used models for studying cytotoxicity. The fibroblast cell line, derived from human skin, represents normal healthy cells, while the MCF-7 cell line, derived from human breast adenocarcinoma, represents malignant cells. The cytotoxicity of complexes (1) and (2) was assessed by incubating varying concentrations of the complexes (ranging from 0 to 200 µg/mL) with the fibroblast and MCF-7 cell lines for 24 h. Control groups of fibroblast and MCF-7 cell lines were cultured

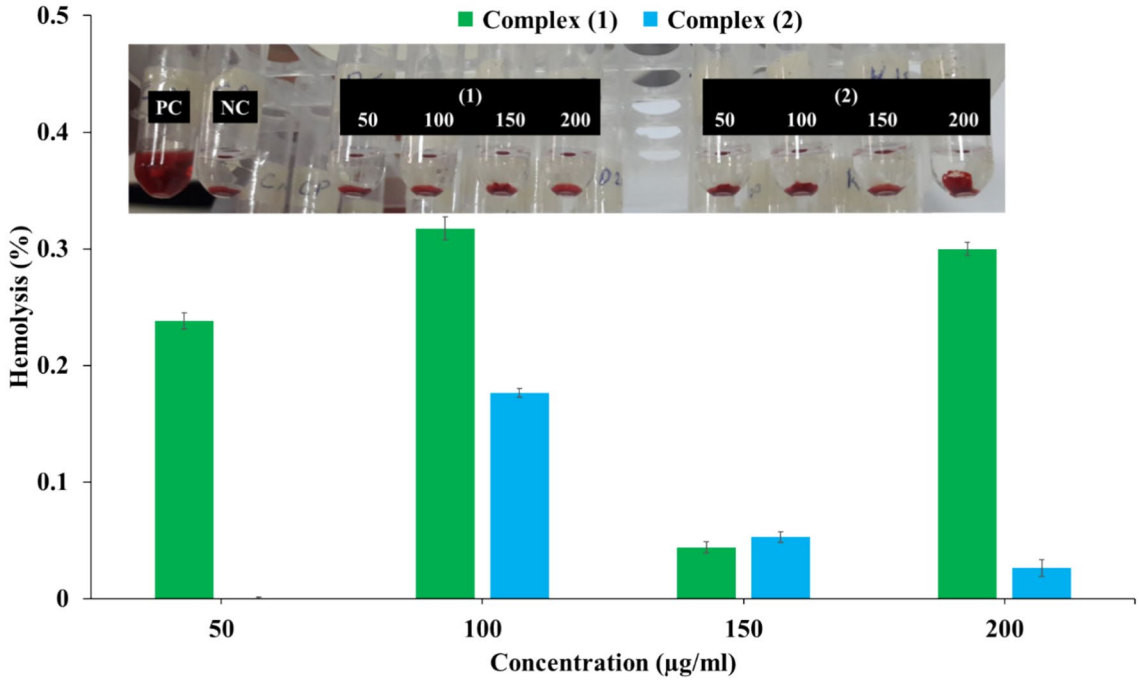

Fig. 12. Hemolytic index of complexes (1) and (2).

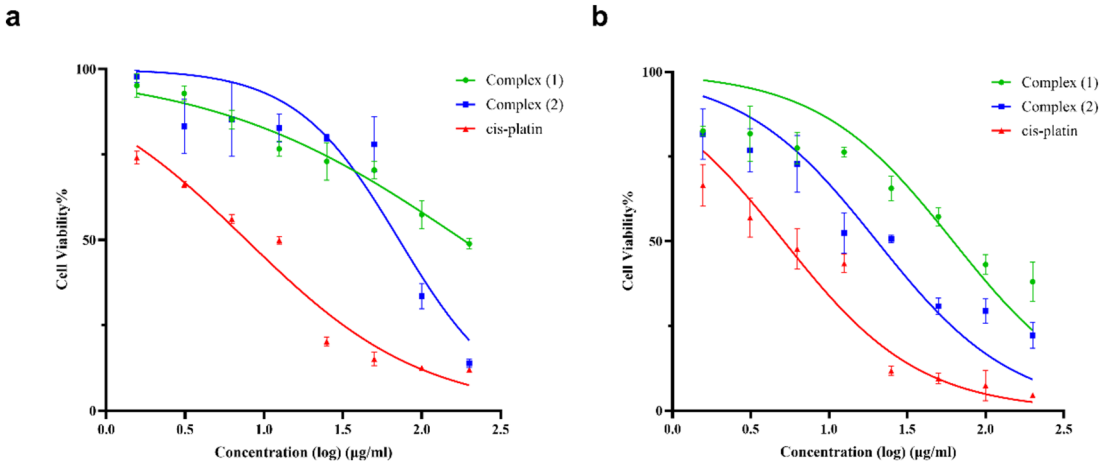

Fig. 13. MTT assay of fibroblast (**a**) and MCF-7 (**b**).

without any compound addition and cisplatin as positive control with equal concentrations of complexes. As shown in Fig. 13, the results indicate that the cytotoxicity of both complexes is concentration-dependent. Higher concentrations result in lower absorbance values, indicating decreased cell viability and increased cytotoxicity. The IC_{50} values, representing the concentration required to inhibit 50% of cell growth, were calculated for both complexes and cisplatin in the fibroblast and MCF-7 cell lines. The IC_{50} values for the fibroblast cell line were determined to be 183 µg/mL for complex (1), 71.91 µg/mL for complex (2), and 7.72 µg/mL for cisplatin (Fig. 13a). In contrast, the IC_{50} values for the MCF-7 cell line were 62.03 µg/mL for complex (1), 20.22 µg/mL for complex (2), and 5.14 µg/mL for cisplatin (Fig. 13b). The comparative analysis indicates that in the fibroblast cell line, both complexes demonstrate decreased cytotoxicity compared to cisplatin. Notably, complex (1) exhibits the lowest toxicity, followed by complex (2), suggesting a heightened safety profile of the copper complexes in normal cells relative to cisplatin. Complex (1) displays the least toxicity, indicating potential higher biocompatibility. In the MCF-7 cell line, cisplatin demonstrated the most potent anticancer activity with the lowest IC_{50} value, indicating its highest growth inhibition against malignant breast cancer cells. Complex (2) exhibited moderate anticancer activity with a lower IC_{50} value than complex (1), but higher than cisplatin. In conclusion, while cisplatin remains the most effective agent against MCF-7 cells, both synthesized copper complexes, particularly complex (1), show a significantly reduced toxicity profile in normal fibroblast cells. Complex (2) provides a

balance with relatively lower toxicity in normal cells compared to cisplatin and higher cell growth inhibition in cancer cells compared to complex (1).

Antibacterial activity

The antibacterial properties of Cu-complexes have been extensively studied in recent years. These complexes have shown promising activity against both Gram-negative and Gram-positive bacteria. The mechanism of action involves the production of ROS such as H_2O_2, O^{2-}, and ·OH, which can induce cell death in bacteria[80–83]. The bacterial cell wall, composed of polysaccharides and peptidoglycans, plays a crucial role in protection. Gram-negative bacteria have a thinner layer of peptidoglycan compared to Gram-positive bacteria[84,85]. Cu-complexes can penetrate the bacterial cell membrane and disrupt the structure by converting to Cu^{+} and Cu^{2+} ions in the presence of a bacterial culture medium[80,86,87]. The size of Cu-complexes is an important factor in their efficacy against bacteria; smaller complexes have higher permeability, allowing them to exert greater toxicity against bacterial cells. Direct contact between bacteria and Cu-containing surfaces can lead to bacterial destruction through contact-killing, which involves the transfer of electrical charge to the bacterial cell membrane[88]. Additionally, Cu-complexes can denature proteins, further contributing to bacterial cell death[89,90]. In the evaluation of the antibacterial efficacy of two novel copper complexes against *E. coli* and *S. aureus* strains, both disk diffusion and broth dilution methods were employed. The MIC values obtained through broth dilution assays revealed that complex (1) exhibited a MIC of 250 µg/mL against *E. coli* (Fig. 14a), while complex (2) demonstrated a MIC of 500 µg/mL (Fig. 14b). In comparison, the reference antibiotic gentamicin displayed superior potency with a MIC of 2 µg/mL against the same strain (Fig. 14c). When tested against *S. aureus*, complex (1) showed an MIC of 1 mg/mL (Fig. 14a), whereas complex (2) exhibited a lower MIC of 500 µg/mL (Fig. 14b). Gentamicin maintained its superior antibacterial activity against *S. aureus* with an MIC of 8 µg/mL (Fig. 14c). These findings indicate a significantly lower antibacterial potency of both synthesized complexes compared to the standard antibiotic. Corroborating the broth dilution results, the disk diffusion assays demonstrated in Fig. 14d that both complexes at concentrations of 1.5 and 2 mg/mL failed to produce observable inhibition zones. In contrast, gentamicin exhibited pronounced inhibition zones, further confirming its superior antibacterial efficacy. The collective data from both methodologies consistently indicate that the synthesized copper complexes possess substantially weaker antibacterial activity compared to the reference antibiotic. The absence of growth inhibition zones in the disk diffusion assays, coupled with the notably higher MIC values, suggests that these complexes do not demonstrate sufficient antibacterial potency to be considered viable candidates for further development as antimicrobial agents. These findings underscore the challenges in developing novel metal-based antibacterial compounds and highlight the need for further structural modifications or alternative strategies to enhance the antibacterial efficacy of such complexes.

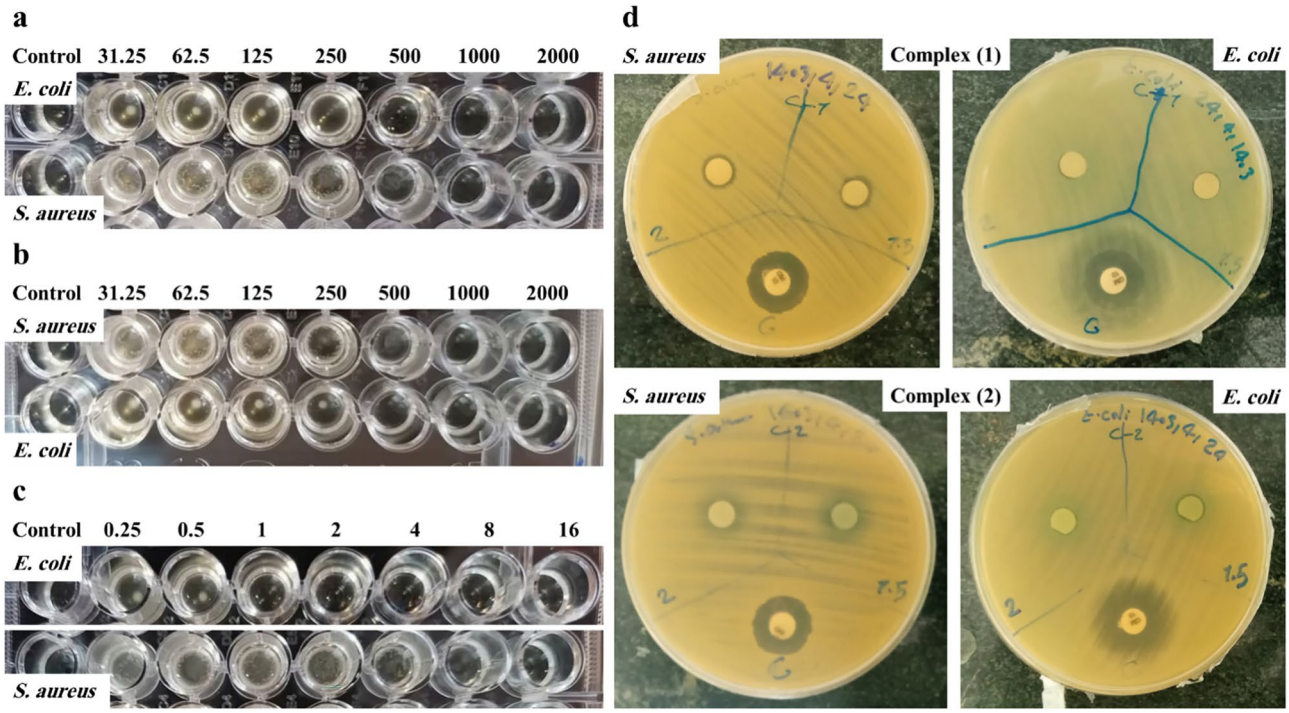

Fig. 14. Antibacterial activity: broth dilution method for complexes (1) (**a**) and (2) (**b**), and gentamicin (**c**); disc diffusion method for complexes (1) and (2), and gentamicin (**d**) against *E. coli* and *S. aureus*.

Conclusion

This study aimed to explore a novel class of Cu^{2+} complexes synthesized through sonochemical methods, focusing on their structural, spectroscopic, and biological properties. The research successfully demonstrated that the synthesized complexes, $[Cu(L)(L')(H_2O)_2]$ (1) and $[Cu(L)(Im)H_2O]$ (2), possess unique structural features and significant biological activities. Both complexes exhibited zero-dimensional supramolecular networks primarily stabilized by hydrogen bonding and π–π stacking interactions, as revealed by single-crystal X-ray structure analysis and other spectroscopic techniques. The findings from this research contribute to the existing knowledge in several ways. Firstly, the sonochemical synthesis approach proved to be effective in creating nanostructured Cu^{2+} complexes with consistent phase identities and structural regularity compared to conventional methods. Secondly, the biological evaluation showed that these complexes have remarkable antioxidant, and non-hemolytic properties, indicating their potential for biomedical applications. Particularly, their low cytotoxicity towards fibroblast and MCF-7 cell lines underscores their suitability for therapeutic uses, including targeted drug delivery and cancer treatment. The theoretical implications of these findings extend to the field of coordination and supramolecular chemistry, providing new insights into the design and synthesis of metal complexes with diverse biomedical and pharmaceutical applications. Practically, the demonstrated biological activities suggest that these complexes could be developed as multifunctional agents in medical and material science fields and components of drug delivery systems. However, the study has some limitations. The in vitro evaluations, while promising, need to be complemented with extensive in vivo studies to fully ascertain the biocompatibility and therapeutic efficacy of these complexes. Additionally, the mechanisms underlying their biological activities warrant further investigation to optimize their performance for specific applications. Future research directions should focus on detailed in vivo studies and exploring the potential of these complexes in various therapeutic contexts. Investigating their interactions at the molecular level could also reveal more about their functionality and pave the way for designing more efficient derivatives. In conclusion, this research highlights the significant potential of sonochemically synthesized Cu^{2+} complexes in advancing supramolecular chemistry and biomedical sciences. The unique structural characteristics and promising biological activities of these complexes make them valuable candidates for further development in medical and material science applications.

Data availability

The datasets used and/or analysed during the current study available from the corresponding author on reasonable request.

Received: 24 May 2024; Accepted: 5 September 2024
Published online: 12 September 2024

References

1. Lehn, J.-M. Supramolecular chemistry: Where from? Where to?. *Chem. Soc. Rev.* **46**, 2378–2379 (2017).
2. Lampard, E. V. *et al.* Dye displacement assay for saccharides using benzoxaborole hydrogels. *ChemistryOpen* **7**, 266–268 (2018).
3. Williams, G. T. *et al.* Boronate ester cross-linked PVA hydrogels for the capture and H_2O_2-mediated release of active fluorophores. *Chem. Commun.* **56**, 5516–5519 (2020).
4. Crane, B. C. *et al.* The development of a continuous intravascular glucose monitoring sensor. *J. Diabetes Sci. Technol.* **9**, 751–761 (2015).
5. Lehn, J. M. Cryptates: The chemistry of macropolycyclic inclusion complexes. *Acc. Chem. Res.* **11**, 49–57 (1978).
6. Patrick, C. & Prosser, G. A molecular complex of benzene and hexafluorobenzene. *Nature* **187**, 1021–1021 (1960).
7. Lawrey, D. M. & McConnell, H. A Spectroscopic study of the benzene-s-trinitrobenzene molecular complex1. *J. Am. Chem. Soc.* **74**, 6175–6177 (1952).
8. Levine, W. G. & Peisach, J. Mechanism of iron stimulation of the enzymatic activity of ceruloplasmin. *Nature* **207**, 406–407 (1965).
9. Tusa, J. K. & He, H. Critical care analyzer with fluorescent optical chemosensors for blood analytes. *J. Mater. Chem.* **15**, 2640–2647 (2005).
10. Gascon, J., Corma, A., Kapteijn, F. & Llabres i Xamena, F. X. Metal organic framework catalysis: Quo vadis?. *ACS Catal.* **4**, 361–378 (2014).
11. Yan, X. *et al.* Light-emitting superstructures with anion effect: Coordination-driven self-assembly of pure tetraphenylethylene metallacycles and metallacages. *J. Am. Chem. Soc.* **138**, 4580–4588 (2016).
12. Ahmad, N., Younus, H. A., Chughtai, A. H. & Verpoort, F. Metal–organic molecular cages: Applications of biochemical implications. *Chem. Soc. Rev.* **44**, 9–25 (2015).
13. Wang, C. *et al.* Thermoresponsive polymeric nanoparticles based on poly (2-oxazoline) s and tannic acid. *J. Polym. Sci. Part A Polym. Chem.* **56**, 1520–1527 (2018).
14. Caulder, D. L. & Raymond, K. N. Supermolecules by design. *Acc. Chem. Res.* **32**, 975–982 (1999).
15. Beheshti, A. *et al.* Synthesis, structural characterization, antibacterial activity and selective dye adsorption of silver (I)-based coordination polymers by tuning spacer length and binding mode of chromate anion. *J. Solid State Chem.* **287**, 121322 (2020).
16. Biedermann, F. & De Cola, L. Porous supramolecular materials: The importance of emptiness. *Supramol. Chem.* **30**, 166–168 (2018).
17. Pöthig, A. & Casini, A. Recent developments of supramolecular metal-based structures for applications in cancer therapy and imaging. *Theranostics* **9**, 3150 (2019).
18. Casini, A., Woods, B. & Wenzel, M. *The Promise of Self-Assembled 3D Supramolecular Coordination Complexes for Biomedical Applications*, Vol. 56. 14715–14729 (ACS Publications, 2017).
19. Saha, M. K., Dey, D. K., Samanta, B., Edwards, A. J., Clegg, W. & Mitra, S. Synthesis, structure and magnetic properties of a mononuclear Cu (II) complex with a NNO donor Schiff base ligand and its oxalato-and oxamidato-bridged dinuclear complexes. *Dalton Transactions*, 488–492 (2003).
20. Boghaei, D. M., Bezaatpour, A. & Behzad, M. Synthesis, characterization and catalytic activity of novel monomeric and polymeric vanadyl Schiff base complexes. *J. Mol. Catal. A Chem.* **245**, 12–16 (2006).
21. Chakraborty, P. *et al.* Role of ligand backbone of tridentate Schiff-base on complex nuclearity and bio-relevant catalytic activities of zinc (II) complexes: Experimental and theoretical investigations. *Inorg. Chim. Acta* **421**, 364–373 (2014).
22. Patil, S. A., Prabhakara, C. T., Halasangi, B. M., Toragalmath, S. S. & Badami, P. S. DNA cleavage, antibacterial, antifungal and anthelmintic studies of Co (II), Ni (II) and Cu (II) complexes of Coumarin Schiff bases: Synthesis and spectral approach. *Spectrochim. Acta Part A Mol. Biomol. Spectrosc.* **137**, 641–651 (2015).

23. Neelakantan, M., Esakkiammal, M., Mariappan, S., Dharmaraja, J. & Jeyakumar, T. Synthesis, characterization and biocidal activities of some Schiff base metal complexes. *Indian J. Pharm. Sci.* **72**, 216 (2010).
24. Salehi, M., Rahimifar, F., Kubicki, M. & Asadi, A. Structural, spectroscopic, electrochemical and antibacterial studies of some new nickel (II) Schiff base complexes. *Inorg. Chim. Acta* **443**, 28–35 (2016).
25. Chandra, S. Synthesis, spectroscopic characterization, molecular modeling and antimicrobial activities of Mn (II), Co (II), Ni (II), Cu (II) complexes containing the tetradentate aza Schiff base ligand. *Spectrochim. Acta Part A Mol. Biomol. Spectrosc.* **103**, 338–348 (2013).
26. Bharti, S. *et al.* Syntheses, characterization, superoxide dismutase, antimicrobial, crystal structure and molecular studies of copper (II) and nickel (II) complexes with 2-((E)-(2, 4-dibromophenylimino) methyl)-4-bromophenol as Schiff base ligand. *J. Mol. Struct.* **1149**, 846–861 (2017).
27. Layek, S. *et al.* Synthesis, spectroscopic and single crystal X-ray studies on three new mononuclear Ni (II) pincer type complexes: DFT calculations and their antimicrobial activities. *J. Mol. Struct.* **1141**, 428–435 (2017).
28. Chandra, S. & Agrawal, S. Spectroscopic characterization of Lanthanoid derived from a hexadentate macrocyclic ligand: Study on antifungal capacity of complexes. *Spectrochim. Acta Part A Mol. Biomol. Spectrosc.* **124**, 564–570 (2014).
29. Kumar, S. *et al.* Co (II), Ni (II), Cu (II) and Zn (II) complexes of Schiff base ligands: Synthesis, characterization, DFT, in vitro antimicrobial activity and molecular docking studies. *Res. Chem. Intermed.* **49**, 939–965 (2023).
30. Tyagi, M., Chandra, S., Akhtar, J. & Chand, D. Modern spectroscopic technique in the characterization of biosensitive macrocyclic Schiff base ligand and its complexes: Inhibitory activity against plantpathogenic fungi. *Spectrochim. Acta Part A Mol. Biomol. Spectrosc.* **118**, 1056–1061 (2014).
31. Sathiyaraj, S., Sampath, K., Butcher, R. J., Pallepogu, R. & Jayabalakrishnan, C. Designing, structural elucidation, comparison of DNA binding, cleavage, radical scavenging activity and anticancer activity of copper (I) complex with 5-dimethyl-2-phenyl-4-[(pyridin-2-ylmethylene)-amino]-1, 2-dihydro-pyrazol-3-one Schiff base ligand. *Eur. J. Med. Chem.* **64**, 81–89 (2013).
32. Khan, S. *et al.* Recent advances and therapeutic journey of Schiff base complexes with selected metals (Pt, Pd, Ag, Au) as potent anticancer agents: A review. *Anti-Cancer Agents Med. Chem.* **22**, 3086–3096 (2022).
33. Chen, G.-J. *et al.* Synthesis, DNA binding, photo-induced DNA cleavage, cytotoxicity and apoptosis studies of copper (II) complexes. *J. Inorg. Biochem.* **105**, 119–126 (2011).
34. Elshafie, H. S., Sadeek, S. A., Camele, I. & Mohamed, A. A. Biochemical characterization of new gemifloxacin schiff base (GMFX-o-phdn) metal complexes and evaluation of their antimicrobial activity against some phyto-or human pathogens. *Int. J. Mol. Sci.* **23**, 2110 (2022).
35. Charef, N. *et al.* Synthesis, characterization, X-ray structures, and biological activity of some metal complexes of the Schiff base 2, 2′-(((azanediylbis (propane-3, 1-diyl)) bis (azanylylidene)) bis (methanylylidene)) diphenol. *Polyhedron* **85**, 450–456 (2015).
36. Rosu, T. *et al.* Synthesis, structural and spectral studies of Cu (II) and V (IV) complexes of a novel Schiff base derived from pyridoxal. Antimicrobial activity. *Polyhedron* **31**, 352–360 (2012).
37. Larionova, J. *et al.* Toward organization of cyano-bridged coordination polymer nanoparticles within an ionic liquid crystal. *Langmuir* **25**, 1138–1147 (2009).
38. El-Sherif, A. A. Synthesis, spectroscopic characterization and biological activity on newly synthesized copper (II) and nickel (II) complexes incorporating bidentate oxygen–nitrogen hydrazone ligands. *Inorg. Chim. Acta* **362**, 4991–5000 (2009).
39. Singh, K., Kumar, Y., Puri, P., Kumar, M. & Sharma, C. Cobalt, nickel, copper and zinc complexes with 1, 3-diphenyl-1H-pyrazole-4-carboxaldehyde Schiff bases: Antimicrobial, spectroscopic, thermal and fluorescence studies. *Eur. J. Med. Chem.* **52**, 313–321 (2012).
40. Tharmaraj, P., Kodimunthiri, D., Sheela, C. & Shanmuga Priya, C. Synthesis, spectral characterization, and antimicrobial activity of copper (II), cobalt (II), and nickel (II) complexes of 3-formylchromoniminopropylsilatrane. *J. Coord. Chem.* **62**, 2220–2228 (2009).
41. Chohan, Z. H. & Farooq, M. Synthesis, characterization, ligational and biological properties of some acylhydrazine derived furanyl and thienyl Schiff bases with Co (II), Cu (II), Ni (II), and Zn (II) metal ions. *Synth. Reactiv. Inorg. Metal-organic Chem.* **31**, 1853–1871 (2001).
42. Chaviara, A. T. *et al.* In vivo anticancer, anti-inflammatory, and toxicity studies of mixed-ligand Cu (II) complexes of dien and its Schiff dibases with heterocyclic aldehydes and 2-amino-2-thiazoline. Crystal structure of [Cu (dien)(Br)(2a–2tzn)](Br)(H2O). *J. Inorg. Biochem.* **99**, 2102–2109 (2005).
43. Zhang, H., Joseph, J., Gurney, M., Becker, D. & Kalyanaraman, B. Bicarbonate enhances peroxidase activity of Cu, Zn-superoxide dismutase: Role of carbonate anion radical and scavenging of carbonate anion radical by metalloporphyrin antioxidant enzyme mimetics. *J. Biol. Chem.* **277**, 1013–1020 (2002).
44. Barve, A. *et al.* Mixed-ligand copper (II) maltolate complexes: Synthesis, characterization, DNA binding and cleavage, and cytotoxicity. *Inorg. Chem.* **48**, 9120–9132 (2009).
45. Rajendiran, V. *et al.* Mixed-ligand copper (II)-phenolate complexes: Effect of coligand on enhanced DNA and protein binding, DNA cleavage, and anticancer activity. *Inorg. Chem.* **46**, 8208–8221 (2007).
46. Nagane, R., Chikira, M., Oumi, M., Shindo, H. & Antholine, W. E. How amino acids control the binding of Cu (II) ions to DNA: Part III. A novel interaction of a histidine complex with DNA. *J. Inorg. Biochem.* **78**, 243–249 (2000).
47. Marzano, C., Pellei, M., Tisato, F. & Santini, C. Copper complexes as anticancer agents. *Anti-Cancer Agents Med. Chem.* **9**, 185–211 (2009).
48. Singh, N. K., Singh, S. B. & Shrivastav, A. Antitumour and immunomodulatory effects of Cu (II) complexes of thiobenzyhdrazide. *Metal-Based Drugs* **9**, 109–118 (2002).
49. Sheldrick, G. M. SHELXT–Integrated space-group and crystal-structure determination. *Acta Crystallogr. Sect. A Found. Adv.* **71**, 3–8 (2015).
50. Blatov, V. A., Shevchenko, A. P. & Proserpio, D. M. Applied topological analysis of crystal structures with the program package ToposPro. *Crystal Growth Des.* **14**, 3576–3586 (2014).
51. Bersuder, P., Hole, M. & Smith, G. Antioxidants from a heated histidine-glucose model system. I: Investigation of the antioxidant role of histidine and isolation of antioxidants by high-performance liquid chromatography. *J. Am. Oil Chem. Soc.* **75**, 181–187 (1998).
52. Can, M., Demirci, S., Sunol, A. K. & Sahiner, N. An amino acid, L-Glutamic acid-based metal-organic frameworks and their antibacterial, blood compatibility, biocompatibility, and sensor properties. *Microporous Mesoporous Mater.* **309**, 110533 (2020).
53. Lau, C. *et al.* Cytotoxic activities of *Coriolus versicolor* (Yunzhi) extract on human leukemia and lymphoma cells by induction of apoptosis. *Life Sci.* **75**, 797–808 (2004).
54. Szliszka, E., Czuba, Z. P., Mazur, B., Paradysz, A. & Krol, W. Chalcones and dihydrochalcones augment TRAIL-mediated apoptosis in prostate cancer cells. *Molecules* **15**, 5336–5353 (2010).
55. Spackman, M. A. & Jayatilaka, D. Hirshfeld surface analysis. *CrystEngComm* **11**, 19–32 (2009).
56. Melvin, M. K., Skelton, B. W., Eggers, P. K. & Raston, C. L. Synthesis, crystallization and Hirshfeld surface analysis of transition metal carboxylate pentapyridines. *CrystEngComm* **24**, 57–69 (2022).
57. Hayati, P., Rezvani, A. R., Morsali, A. & Retailleau, P. Ultrasound irradiation effect on morphology and size of two new potassium coordination supramolecule compounds. *Ultrason. Sonochem.* **34**, 195–205 (2017).

58. Moghzi, F. & Soleimannejad, J. Sonochemical synthesis of a new nano-sized barium coordination polymer and its application as a heterogeneous catalyst towards sono-synthesis of biodiesel. *Ultrason. Sonochem.* **42**, 193–200 (2018).
59. Bahsis, L. *et al.* Copper (II)-dipicolinate-mediated clickable azide–alkyne cycloaddition in water as solvent. *J. Coord. Chem.* **71**, 633–643 (2018).
60. Orhan, O. *et al.* Syntheses of crystal structures and in vitro cytotoxic activities of new copper (II) complexes of pyridine-2, 6-dicarboxylate. *J. Coord. Chem.* **68**, 4003–4016 (2015).
61. Mistri, S., Zangrando, E. & Manna, S. C. Cu (II) complexes of pyridine-2, 6-dicarboxylate and N-donor neutral ligands: Synthesis, crystal structure, thermal behavior, DFT calculation and effect of aromatic compounds on their fluorescence. *Inorg. Chim. Acta* **405**, 331–338 (2013).
62. Nakamoto, K. *Infrared and Raman Spectra of Inorganic and Coordination Compounds, Part B: Applications in Coordination, Organometallic, and Bioinorganic Chemistry* (Wiley, 2009).
63. Teixeira, J., Gaspar, A., Garrido, E. M., Garrido, J. & Borges, F. Hydroxycinnamic acid antioxidants: An electrochemical overview. *BioMed Res. Int.* **2013**, 251754 (2013).
64. Rubab, M., Chelliah, R. & Oh, D.-H. Screening for antioxidant activity: Diphenylpicrylhydrazine (DPPH) assay. In *Methods in Actinobacteriology* 453–454 (Springer, 2022).
65. Piszcz, P., Tomaszewska, M. & Głód, B. K. Estimation of the total antioxidant potential in the meat samples using thin-layer chromatography. *Open Chem.* **18**, 50–57 (2020).
66. Sundaram Sanjay, S. & Shukla, A. K. *Potential Therapeutic Applications of Nano-antioxidants* 83–99 (Springer, 2021).
67. Qin, Z., Liu, H.-M., Gu, L.-B., Sun, R.-C. & Wang, X.-D. Lignin as a natural antioxidant: Property-structure relationship and potential applications. *Reactive and Functional Polymers Volume One: Biopolymers, Polyesters, Polyurethanes, Resins and Silicones*, 65–93 (2020).
68. Marković, Z. Study of the mechanisms of antioxidative action of different antioxidants. *J. Serb. Soc. Comput. Mech.* **10**, 135–150 (2016).
69. Gulcin, İ & Alwasel, S. H. DPPH radical scavenging assay. *Processes* **11**, 2248 (2023).
70. Sharifi-Rad, M. *et al.* Lifestyle, oxidative stress, and antioxidants: Back and forth in the pathophysiology of chronic diseases. *Front. Physiol.* **11**, 694 (2020).
71. Davalli, P., Mitic, T., Caporali, A., Lauriola, A. & D'Arca, D. ROS, cell senescence, and novel molecular mechanisms in aging and age-related diseases. *Oxid. Med. Cell. Longev.* **2016**, 3565127 (2016).
72. Leyane, T. S., Jere, S. W. & Houreld, N. N. Oxidative stress in ageing and chronic degenerative pathologies: Molecular mechanisms involved in counteracting oxidative stress and chronic inflammation. *Int. J. Mol. Sci.* **23**, 7273 (2022).
73. Liu, Z. *et al.* Role of ROS and nutritional antioxidants in human diseases. *Front. Physiol.* **9**, 477 (2018).
74. George, S. & Abrahamse, H. Redox potential of antioxidants in cancer progression and prevention. *Antioxidants* **9**, 1156 (2020).
75. Xing, F. *et al.* The relationship of redox with hallmarks of cancer: The importance of homeostasis and context. *Front. Oncol.* **12**, 862743 (2022).
76. Förstermann, U. & Sessa, W. C. Nitric oxide synthases: Regulation and function. *Eur. Heart J.* **33**, 829–837 (2012).
77. Weber, M. *et al.* Blood-contacting biomaterials: In vitro evaluation of the hemocompatibility. *Front. Bioeng. Biotechnol.* **6**, 99 (2018).
78. Phillips, J. & Henderson, A. C. Hemolytic anemia: Evaluation and differential diagnosis. *Am. Fam. Physician* **98**, 354–361 (2018).
79. Farooq, M. *et al.* Synthesis, characterization and modification of Gum Arabic microgels for hemocompatibility and antimicrobial studies. *Carbohydr. Polym.* **156**, 380–389 (2017).
80. Ma, X., Zhou, S., Xu, X. & Du, Q. Copper-containing nanoparticles: Mechanism of antimicrobial effect and application in dentistry—A narrative review. *Front. Surg.* **9**, 905892 (2022).
81. Salah, I., Parkin, I. P. & Allan, E. Copper as an antimicrobial agent: Recent advances. *RSC Adv.* **11**, 18179–18186 (2021).
82. Vincent, M., Hartemann, P. & Engels-Deutsch, M. Antimicrobial applications of copper. *Int. J. Hyg. Environ. Health* **219**, 585–591 (2016).
83. Zhuang, Y., Zhang, S., Yang, K., Ren, L. & Dai, K. Antibacterial activity of copper-bearing 316L stainless steel for the prevention of implant-related infection. *J. Biomed. Mater. Res. Part B Appl. Biomater.* **108**, 484–495 (2020).
84. Edis, Z., Haj Bloukh, S., Ashames, A. & Ibrahim, M. Copper-based Nanoparticles, their chemistry and Antibacterial properties: A review. In *Chemistry for a Clean and Healthy Planet*, 401–428 (2019).
85. Yadav, L., Tripathi, R. M., Prasad, R., Pudake, R. N. & Mittal, J. Antibacterial activity of Cu nanoparticles against *E. coli*, *Staphylococcus aureus* and *Pseudomonas aeruginosa*. *Nano Biomed. Eng.* **9**, 9–14 (2017).
86. Sheng, L. *et al.* Deposition of copper nanoparticles on multiwalled carbon nanotubes modified with poly (acrylic acid) and their antimicrobial application in water treatment. *Front. Environ. Sci. Eng.* **9**, 625–633 (2015).
87. Seo, Y. *et al.* Engineering copper nanoparticles synthesized on the surface of carbon nanotubes for anti-microbial and anti-biofilm applications. *Nanoscale* **10**, 15529–15544 (2018).
88. Zhang, X., Yang, C. & Yang, K. Contact killing of Cu-bearing stainless steel based on charge transfer caused by the microdomain potential difference. *ACS Appl. Mater. Interfaces* **12**, 361–372 (2019).
89. Yu-sen, E. L., Vidic, R. D., Stout, J. E., McCartney, C. A. & Victor, L. Y. Inactivation of *Mycobacterium avium* by copper and silver ions. *Water Res.* **32**, 1997–2000 (1998).
90. Mallick, S. *et al.* Iodine-stabilized Cu nanoparticle chitosan composite for antibacterial applications. *ACS Appl. Mater. Interfaces* **4**, 1313–1323 (2012).

Acknowledgements

This work was supported by the Kermanshah University of Medical Sciences and Razi University, Kermanshah, Iran and partial supported by Persian Gulf University and Iran University of Science and Technology.

Author contributions

H. G., and H. D., and K. B., Conceptualization, methodology writing—original draft preparation and S. K., and K. M., writing—original draft preparation, and P. H., and R. C., and E. P. writing—review and editing.

Competing interests

The authors declare no competing interests.

Additional information

Supplementary Information The online version contains supplementary material available at https://doi.org/10.1038/s41598-024-72345-8.

Correspondence and requests for materials should be addressed to H.D., K.B., K.M. or P.H.